Conf-8204113--1

Cross Sections for Inelastic Scattering of Electrons by Atoms - Selected Topics Related to Electron Microscopy*

CONF-8204113--1

DE83 007185

Mitio Inokuti

Argonne National Laboratory, Argonne, Illinois 60439

and

Steven T. Manson

Department of Physics and Astronomy
Georgia State University, Atlanta, Georgia 30303

Abstract

We begin with a resumé of the Bethe theory, which provides a general framework for discussing the inelastic scattering of fast electrons and leads to powerful criteria for judging the reliability of cross-section data. The central notion of the theory is the generalized oscillator strength as a function of both the energy transfer and the momentum transfer, and is the only non-trivial factor in the inelastic-scattering cross section. Although the Bethe theory was initially conceived for free atoms, its basic ideas apply to solids, with suitable generalizations; in this respect, the notion of the dielectric response function is the most fundamental. Topics selected for discussion include the generalized oscillator strengths for the K-shell and L-shell ionization for all atoms with $Z \leq 30$, evaluated by use of the Hartree-Slater potential. As a function of the energy transfer, the generalized oscillator strength most often shows a non-monotonic structure near the K-shell and L-shell thresholds, which has been interpreted as manifestations of electron-wave propagation through atomic fields. For molecules and solids, there are additional structures due to the scattering of ejected electrons by the fields of other atoms.

Key words: Bethe theory, inner shells, generalized oscillator strength, momentum transfer, cross section, inelastic scattering, non-hydrogenic, systematics

Running title: Cross sections for inelastic scattering

Correspondent: Mitio Inokuti, Argonne National Laboratory, Argonne, Illinois 60439 (312) 972-4186

*Work performed under the auspices of the U.S. Department of Energy.

Conf-8204113--1

Cross Sections for Inelastic Scattering of Electrons by Atoms - Selected Topics Related to Electron Microscopy*

Mitio Inokuti

Argonne National Laboratory, Argonne, Illinois 60439

and

Steven T. Manson

Department of Physics and Astronomy
Georgia State University, Atlanta, Georgia 30303

Abstract

We begin with a resumé of the Bethe theory, which provides a general framework for discussing the inelastic scattering of fast electrons and leads to powerful criteria for judging the reliability of cross-section data. The central notion of the theory is the generalized oscillator strength as a function of both the energy transfer and the momentum transfer, and is the only non-trivial factor in the inelastic-scattering cross section. Although the Bethe theory was initially conceived for free atoms, its basic ideas apply to solids, with suitable generalizations; in this respect, the notion of the dielectric response function is the most fundamental. Topics selected for discussion include the generalized oscillator strengths for the K-shell and L-shell ionization for all atoms with $Z \leqq 30$, evaluated by use of the Hartree-Slater potential. As a function of the energy transfer, the generalized oscillator strength most often shows a non-monotonic structure near the K-shell and L-shell thresholds, which has been interpreted as manifestations of electron-wave propagation through atomic fields. For molecules and solids, there are additional structures due to the scattering of ejected electrons by the fields of other atoms.

Key words: Bethe theory, inner shells, generalized oscillator strength, momentum transfer, cross section, inelastic scattering, non-hydrogenic, systematics

Running title: Cross sections for inelastic scattering

Correspondent: Mitio Inokuti, Argonne National Laboratory, Argonne, Illinois 60439 (312) 972-4186

*Work performed under the auspices of the U.S. Department of Energy.

DISCLAIMER

1. Introduction

Throughout the present article, we consider incident electrons at kinetic energies of interest to microscopy, i.e., between a few tens of keV and several MeV. As to targets, we consider first neutral atoms having lower atomic numbers (say, $Z < 30$), and later molecules and solids composed of those atoms. For the majority of the inelastic collisions of electrons with atoms thus delimited, the Bethe theory (Bethe 1930, 1932, 1933) is well justified, and provides a good framework for general understanding and for numerical evaluation of cross sections (Inokuti 1971; Inokuti et al 1978).

A necessary (though not sufficient) condition for the first Born approximation, used in the Bethe theory, is that the mean orbital speed of the atomic electron pertinent to the inelastic collision be small compared to the incident electron speed. For ionization (or excitation) of an inner shell by relativistic electrons, the condition means that the effective charge ζ seen by an atomic electron in that shell be substantially smaller than 137; ζ is somewhat smaller than the atomic number Z, and the condition is fulfilled for moderate Z, (say $Z < 30$). For the lowest incident energies of electrons we consider, the condition is satisfied only for lower Z.

The condition discussed above literally applies to quantitative discussion of cross sections. Even when the condition is not quite fulfilled, however, often results of the first Born approximation are useful; they may be good as qualitative guides and may be reliable to modest precision (say, within a factor of two). This is especially the case for inelastic collisions resulting in an optically allowed transition and in small scattering angles; then, the impact parameter is large and thus the incident electron travels well outside

the target atom. This recognition is readily verifiable in a variety of empirical data, and is in effect expressible in a more rigorous theoretical form (Lassettre et al 1969).

Figure 1 exemplifies differential cross sections plotted against the scattering angle θ. The figure shows the cross sections for collisions of 25-keV electrons with neon, most of the data being taken from Geiger (1964). Notice that all cross sections are peaked at small angles and that the plot is doubly logarithmic. The elastic-collision cross section is virtually flat at small θ, because the interactions between the electron and the atom effectively have a short range in this case. The potential for these interactions decreases with distance r as r^{-4} or more rapidly. The inelastic-collision cross sections depend on θ more strongly and behave as θ^{-2} over a moderate range of θ, showing that the interactions are of long range (due to the instantaneous dipole moment associated with the atomic transition). The potential for these interactions decreases with distance r as slowly as r^{-2}. At larger θ, the θ-dependence of the inelastic-collision cross section is stronger; the onset of the stronger dependence is different for different atomic shells involved. It is the Bethe theory that enables one to see precisely all these features of the cross sections and to understand how they come about.

As a prelude to discussion on cross sections, we may note here certain contrasts between the valence shell and the inner shells. The valence shell has a linear dimension of the standard atomic size, i.e., of the order of the Bohr radius $a_0 = \hbar^2/me^2 = 0.52917 \times 10^{-8}$ cm, and has binding energies of the order of the Rydberg energy $R = me^4/2\hbar^2 = 13.606$ eV. The electronic structure of the valence shell is seriously influenced by subtle effects of many-electron correlations or of the atomic environment (i.e., chemical bonds

and condensed-phase formation). Consequently, experimental spectra of the valence shell are rich in general, and often contain keys for unraveling those subtle effects; theoretical calculation of the cross section for valence-shell excitation or ionization is complicated in general and is often difficult in practice. By contrast, an inner shell has a much smaller linear dimension (of the order of a_0/ζ) and a much greater binding energy (of the order of $\zeta^2 R$). Many-electron correlations or atomic-environment effects influence the electronic structure of an inner shell only modestly. Thus, experimental spectra of the inner shell are governed roughly by the atomic number Z, and therefore often serve as a means of elemental chemical analysis. The simple picture of the inner-shell spectra is often taken for granted, but is in fact subject to a provision. The simple picture is right so long as an ejected electron is much more energetic compared to the potential of its interactions with the ion core left behind and with the atomic environment. Otherwise, the ejected electron is slow enough to see details of the potential, and gives rise to various observable consequences in the inner-shell spectra. Much of the discussion in Section 3 will concern this topic.

The present article is in effect a continuation of an earlier article (Inokuti 1978) also written for the electron microscopist. For the reader of that article, the following will serve as an update with an emphasis on newer findings on inner-shell ionization.

2. Elements of the Bethe Theory

2.1 Basics

Suppose that an electron of speed v collides with an atom and excites it to a higher state, either discrete or continuum, at excitation energy E measured from the ground state. The kinetic energy of the electron then will be reduced by E, which may be called the energy loss (from the incident electron) or the energy transfer (to the target atom). The direction of the electron motion may be deflected by angle θ, which is called the scattering angle.

The first point of Bethe is that the momentum transfer $\hbar\underset{\sim}{K} = \underset{\sim}{p} - \underset{\sim}{p}'$, where $\underset{\sim}{p}$ is the electron momentum before the collision and $\underset{\sim}{p}'$ is the same after the collision, is the key variable for analyzing any collision of fast particles. The magnitude $\hbar K$ is readily calculable from θ, E, and v by use of elementary kinematics. For electron energies not negligible compared to mc^2 = 511 keV, one must use relativistic kinematics.

The notion of the momentum transfer $\hbar K$ may be most easily understandable when one relates it to the notion of the impact parameter b used in classical mechanics. Indeed, the two notions are complementary in the sense that the relation

$$Kb \cong 1 \qquad (1)$$

holds for the majority of collisions. In other words, collisions at large b are called soft or glancing, and result in small K; collisions at small b are called hard or knock-on, and result in large K. Nevertheless, there is a fundamental distinction; the momentum transfer is unambiguously defined in all cases, while the impact parameter is not a quantum-mechanical

observable. [See Section 4.4 of Inokuti 1971 and Bohr 1948.]

For fixed v and E, the momentum transfer $\hbar K$ may take a range of values depending on θ. The smallest value of $\hbar K$ occurs when $\theta = 0$, and is given by

$$\hbar K_{min} \cong E/v. \tag{2}$$

To derive this, one relates the change Δp in the electron momentum p with the change ΔT in the kinetic energy T as $\Delta p = (dp/dT)\Delta T$, sets $\Delta p = \hbar K_{min}$ and $\Delta T = E$, and notes $dT/dp = v$. The derivation, as well as the result [Eq. (2)], is correct in both relativistic and non-relativistic kinematics. Notice that $\hbar K_{min}$ for any inelastic collision is never vanishing, although it becomes smaller and smaller with increasing v or with decreasing E. The largest value of $\hbar K$ for fixed v occurs when $\theta = \pi$, and is about twice the incident momentum, i.e.,

$$\hbar K_{max} \cong 2mv/(1-\beta^2)^{\frac{1}{2}}, \tag{3}$$

where $\beta = v/c$. Thus, $\hbar K_{max}$ is in general large and increases without bounds as $v \to c$.

The second point of Bethe concerns the differential cross section for energy transfer values between E and E + dE

$$d\sigma_E = 4a_0^2(p'/p)(Ka_0)^{-4}|\eta_E(K)|^2\, 2\pi\sin\theta d\theta, \tag{4}$$

where $\eta_E(K)$ is an atomic matrix element

$$\eta_E(K) = (E|\sum_{j=1}^{Z} \exp(i\underset{\sim}{K}\cdot\underset{\sim}{r}_j)|0) \tag{5}$$

taken between the excited state $(E|$ and the ground state $|0)$, $\underset{\sim}{r}_j$ being the position of the jth atomic electron. The quantity $|\eta_E(K)|^2$ is called a form factor for inelastic scattering, and may be taken as an even

function of scalar K, so long as the target atoms or molecules are randomly oriented. Equations (4) and (5), as well as several equations to follow, are written specifically for non-relativistic speeds v, for the sake of compact expression. Notice that $d\sigma_E$ has the dimension area^2 energy,$^{-1}$ and $|(\eta_E(K)|^2$ has the dimension energy^{-1}.

We may rewrite Eq. (4) to express $d\sigma_E$ in terms of the momentum transfer $\hbar K$ or other related variables. For instance, one may introduce a variable with the energy dimension, i.e.,

$$Q = (\hbar K)^2/2m \tag{6}$$

and write

$$d\sigma_E = (2\pi e^4/mv^2)|\eta_E(K)|^2 \; Q^{-2} \, dQ. \tag{7}$$

Here it is appropriate to recall the Rutherford formula, which applies to collisions of two free charged particles. Specifically for a collision of an electron with a free and stationary electron, the Rutherford cross section reads

$$d\sigma_R = (2\pi e^4/mv^2) \; Q^{-2} \, dQ, \tag{8}$$

and Q represents in this hypothetical instance the kinetic energy of the recoiled electron. Thus the meaning of the form factor $|\eta_E(K)|^2$ becomes clear; it represents the ratio of the atomic cross section $d\sigma_E$ to the Rutherford cross section. It is the only nontrivial factor in $d\sigma_E$ in the sense that its evaluation by means of Eq. (5) presumes knowledge of atomic structure. To summarize, we owe to Bethe (then twenty-four years old) the crucial recognition that $d\sigma_E$ factorizes into the Rutherford cross section (which depends on the incident-particle variables only) and the

form factor (which depends on the momentum transfer $\hbar K$ but not explicitly on the incident speed v or any other incident particle variable). For more detailed commentary, see Inokuti 1971 and Inokuti 1978.

Finally, the generalized oscillator strength df(K,E)/dE per unit range of E is defined by

$$df(K,E)/dE = (E/Q)\left|\eta_E(K)\right|^2 . \tag{9}$$

Equivalently, we may write

$$df(K,E)/dE = (E/R)(Ka_0)^{-2}\left|\eta_E(K)\right|^2 . \tag{10}$$

The equivalence of Eq. (10) with Eq. (9) is apparent as soon as one recalls that $Ra_0^2 = (me^4/2\hbar^2)(\hbar^2/me^2)^2 = \hbar^2/2m$. The term "generalized oscillator strength" is another innovation of Bethe. As $K \to 0$, it reduces to the optical (dipole) oscillator strength, which governs the light absorption and practically all optical properties of the atom under consideration. For the basics of photoabsorption by atoms, see Fano and Cooper (1968), Manson (1976), Manson (1977), Manson (1978), and Manson and Dill (1978).

2.2 The Bethe Surface

The main object of study is the form factor $\left|\eta_E(K)\right|^2$ or the generalized oscillator-strength density df(K,E)/dE as a function of both $\hbar K$ and E. To make this point clear, Inokuti (1971) used the term "Bethe surface."

We have already discussed the connection with the photoabsorption, which corresponds to the limit ($K \to 0$) we discussed at the end of the last Subsection 2.1.

At larger E values, df(K,E)/dE substantially differs from zero only when Q of Eq. (6) nearly equals E and far exceeds an atomic-shell binding energy. Then, df(K,E)/dE shows a marked peak at those values of K and E which correspond to free-electron collision thus satisfying the relation Q = E. Inokuti (1971) called the peak the Bethe ridge, and emphasized its universal occurrence.

Figure 2 shows the Bethe surface for atomic hydrogen (Inokuti 1971). Figure 3 shows two examples that have been determined by experiment (Lahmam-Bennani et al, 1979, 1980).

The study of the Bethe surface is a rich subject with many applications and implications to diverse phenomena. Just to name several examples, we may start with sum rules, which usually mean theorems on the integrals involving df(K,E)/dE with respect to E (including sums over discrete spectra), at fixed K. These sum rules (Section 3.3 of Inokuti 1971) are often useful as control on data. There are also theorems on the integrals involving df(K,E)/dE with respect to K, at fixed E. (See Section IIE of Inokuti et al, 1978, and Matsuzawa et al, 1979). If the Bethe surface is drawn on the plane with Cartesian axes representing E and ln K, then the volume under the surface delimited by appropriate kinematic limits represents the stopping power of the target atom for any fast charged particle (Bethe 1930, and Section 4.3 of Inokuti 1971). The shape of the Bethe ridge is a reflection of electron binding in atoms, or more precisely, the electron momentum distribution, and is connected with the Compton profile, i.e., the spectral distribution of high-energy

photons scattered by atomic electrons (Bonham and Wellenstein 1973, Wong et al 1975, Barlas et al 1977, and Lahmam-Bennani et al (1979, 1980). Finally, the so-called (e,2e) measurements, i.e., coincidence measurements of scattered electrons and ejected electrons resulting from collisions corresponding to the Bethe ridge, represent an area of many recent studies (McCarthy and Weigold 1976).

2.3 Integrated Cross Sections and Their Systematics

The third point of Bethe concerns the cross section integrated over all scattering angles. Starting with Eqs. (4)-(7) and using general properties of the form factor or of the generalized oscillator strength, one can show that

$$\sigma_E = 8\pi a_0^2 (R/mv^2)(M_E^2 X + C_E), \tag{11}$$

where

$$X = \ln[\beta^2/(1 - \beta^2)] - \beta^2, \tag{12}$$

and M_E^2 and C_E are atomic properties derivable from $df(K,E)/dE$. What is most important here is that the dependence of σ_E on the electron speed $v = \beta c$ is analytically given and is universal for all targets.

As a consequence, the total inelastic-collision cross section σ_{tot}, i.e., the sum of all inelastic-collision cross sections, is given by a formula of the same general structure, i.e.,

$$\sigma_{tot} = 8\pi a_0^2 (R/mv^2)(M_{tot}^2 X + C_{tot}), \tag{13}$$

where M_{tot}^2 and C_{tot} are atomic properties that often allow accurate evaluation. (See Section 4.3 of Inokuti 1971 and Inokuti et al 1967). An application of this result is now demonstrated in Fig. 4 and Fig. 5 (taken

from Inokuti et al 1981). Figure 4 shows σ_{tot} for 50-keV electron for all atoms with $Z \leq 38$. Notice the periodic variation with Z, due to the well-known shell structure of atoms. Figure 5 shows the mean energy transfer E_{av} per inelastic collision, for 50-keV electrons (solid line) and for any highly relativistic charged particle (broken line), as functions of Z. As Inokuti (1978) pointed out already, electron microscopists often use theoretical values for σ_{tot} and E_{av} based on the Thomas-Fermi model of atoms. This model treats all atomic electrons as a free-electron gas, disregards the atomic shell structure, and therefore naturally predicts σ_{tot} and E_{av} as smooth functions of Z.

2.4 Condensed Phases

Bethe treated free atoms as target. Extension to free molecules is formally straightforward. In the definition of the matrix element $\eta_E(K)$ [Eq. (5)] molecular eigenfunctions must be used, and the rotational and vibrational degrees of freedom must be accounted for. Despite the complications, the theory remains basically unchanged. For fuller discussion, see Section 3.5 of Inokuti (1971).

Extension to condensed phases began with the work of Fermi (1940), who pointed out what we call the density effect on energy losses. For a relativistic particle traveling through condensed matter, the relevant impact parameter may become so large that there are many medium atoms between the particle and a particular atom that becomes excited. To see this, recall Eqs. (1) and (2); the maximum impact parameter is $1/K_{min} \cong \hbar c/E$, and becomes $2 \times 137\ a_0$ for $E = R$. The medium atoms are instantaneously

polarized by the electric field of the particle and tend to screen the particle interactions with the atom that eventually receives energy. Fermi used a macroscopic description according to electrodynamics, as summarized by Landau and Lifshitz (1960).

More detailed treatments were developed in the 1950's by many workers including Fano (1956), Ferrell (1957), and Nozières and Pines (1959). Special attention was paid to plasmon excitations in metals, which then began to be studied through electron energy-loss measurements. Recent work on plasmon excitation is reviewed by Raether (1980). The following paper by Powell (1982) in the present Conference will include even newer findings.

Here we make only a few remarks. The three major points of Bethe (i.e., the role of the momentum transfer, the factorization of the cross section into the Rutherford factor and the form factor, and the analytic structure of the integrated cross section) all remain true for condensed phases. The form-factor idea is generalized, and it is customary to use the complex dielectric response function $\varepsilon(\underset{\sim}{K},E)$ for describing the effects of electromagnetic perturbation associated with angular frequency $E/\hbar$ and propagation vector K. The function may be interpreted also as the Fourier transform of the electron density fluctuation in the medium. For charged-particle interactions, the quantity $E\ \mathrm{Im}[-1/\varepsilon(\underset{\sim}{K},E)]$ plays the role of the generalized oscillator strength $df(K,E)/dE$.

The use of the complex function $\varepsilon(\underset{\sim}{K},E)$ entails studies on the analytic properties, especially on the integral relations between the real and imaginary parts, called Kramers-Kronig dispersion relations.

Thorough exploitation of these relations has been carried out for several instances, e.g., metallic aluminum (Shiles et al 1980), but only for data at K = 0.

3. Selected Topics

3.1 Generalized Oscillator Strengths for Inner Shells of Atoms: Methods of Calculations

Earlier calculations on the generalized oscillator strengths of inner shells and related quantities were based on the hydrogenic approximation (Walske 1952, Walske 1956, and Khandelwal and Merzbacher 1966, to name just three examples). In this scheme, one uses for one-electron eigenfunctions for both the initial state and the final state hydrogenic functions, but accounts for the screening by other electrons by means of a suitable effective nuclear charge by an adjustment of the energy scale to fit the experimental ionization threshold. Then, the generalized oscillator strengths may be readily evaluated analytically. Yet, the procedure is intrinsically unrealistic for values of the energy transfer E comparable with the ionization threshold; this deficiency is serious because much of the strength lies precisely at those E values for small and moderate K values.

Manson (1972a, 1972b) initiated more realistic calculations, within the one-electron orbital picture. In this picture, one approximates the ground state $|0)$ of the whole atom by a suitably antisymmetrized product of one-electron orbitals of the form $r^{-1}P_{n\ell}(r)\, Y_{\ell m}(\theta,\phi)$, where (r, θ, ϕ) are the spherical coordinates of an atomic electron, $P_{n\ell}(r)$ is the radial function with the principal quantum number n and the orbital angular-momentum quantum number ℓ, $Y_{\ell m}(\theta, \phi)$ is the spherical harmonic, and m is the magnetic quantum number. At the same time, one approximates the excited state $|E)$ in the continuum by $r^{-1}P_{\varepsilon\ell'}(r)\, Y_{\ell m}(\theta, \phi)$, where $P_{\varepsilon\ell'}(r)$ is the radial function representing an electron ejected with

kinetic energy ϵ and angular momentum ℓ'. For the ionization of the $n\ell$ shell having the binding energy $I_{n\ell}$, ϵ is related to the energy transfer E by

$$E = \epsilon + I_{n\ell}. \tag{14}$$

For the transition of an electron from the $n\ell$ subshell to the ionized state, one may write the atomic matrix element squared as

$$|\eta_E(K)|^2 = (2\ell'+1)\Sigma_\lambda(2\lambda+1)\left|\begin{pmatrix}\ell' & \lambda & \ell\\ 0 & 0 & 0\end{pmatrix}\right|^2 [R(\epsilon,\ell',n,\ell,\lambda,K)]^2, \tag{15}$$

where $\begin{pmatrix}\ell' & \lambda & \ell\\ 0 & 0 & 0\end{pmatrix}$ is the Wigner 3j symbol, the sum over the index λ runs from $-|\ell-\ell'|$ to $\ell+\ell'$ in steps of 2, and $R(\epsilon,\ell',n,\ell,\lambda,K)$ is the radial matrix element defined by

$$R(\epsilon,\ell',n,\ell,\lambda,K) = \int_0^\infty P_{\epsilon\ell'}(r) j_\lambda(Kr) P_{n\ell}(r)\,dr, \tag{16}$$

$j_\lambda(Kr)$ being the spherical Bessel function of the λth order. In Eq. (15), the radial matrix element is the only quantity that depends on the dynamics of atomic electron, all the other factors being geometric, i.e., dependent only upon angular-momentum quantum numbers.

The most crucial part of the calculation is the determination of the radial functions P's. The function $P_{n\ell}(r)$ for a bound state with a discrete eigenenergy $\epsilon_{n\ell} < 0$ satisfies the equation

$$\frac{\hbar^2}{2m}\frac{d^2P_{n\ell}}{dr^2} + \left[\epsilon_{n\ell} - V(r) - \frac{\hbar^2\ell(\ell+1)}{2mr^2}\right]P_{n\ell} = 0, \tag{17}$$

behaves as $r^{\ell+1}$ for small r, and vanishes rapidly for large r so that it may be normalized as

$$\int_0^\infty [P_{n\ell}(r)]^2 \, dr = 1. \tag{18}$$

In Eq. (17), V(r) is the potential of the field of force seen by the electron, and the field is due to all the other atomic electrons and the nucleus. For a neutral atom of atomic number Z, the general limiting behavior is

$$V(r) \cong -Ze^2/r \quad \text{for} \quad r \cong 0, \tag{19}$$

and

$$V(r) \cong -e^2/r \quad \text{for} \quad r \to \infty. \tag{20}$$

In many calculations including Manson's, V(r) is determined through a version of self-consistent field theories, called the Hartree-Slater method.

The function $P_{\varepsilon\ell}(r)$ for a final, continuum state with energy $\varepsilon > 0$ satisfies the equation

$$\frac{\hbar^2}{2m} \frac{d^2P_{\varepsilon\ell}}{dr^2} + \left[\varepsilon - V(r) - \frac{\hbar^2\ell(\ell+1)}{2mr^2}\right] P_{\varepsilon\ell} = 0, \tag{21}$$

behaves as $r^{\ell+1}$ for small r, and is to be normalized as

$$\int_0^\infty P_{\varepsilon\ell}(r) \, P_{\varepsilon'\ell}(r) \, dr = \delta(\varepsilon-\varepsilon'). \tag{22}$$

Notice that the same potential V(r) is used in Eq. (21) as in Eq. (17); the use of the same V(r) not only simplifies the calculation, but also guarantees its internal self-consistency.

The contrast of the modern calculation with the hydrogenic approximation is seen in the choice of the potential V(r). The hydrogenic approximation amounts to using

$$V_{Hyd}(r) = -Z_{eff}\, e^2/r + V_0, \qquad (23)$$

where Z_{eff} and V_0 are two adjustable parameters. This potential $V_{Hyd}(r)$ satisfies neither of the two limiting forms, Eqs. (19) and (20). Therefore, the hydrogenic approximation can give no realistic behavior of radial wavefunctions for $r \cong 0$ or for $r \to \infty$, nor trustworthy results for properties depending upon the behavior of the wavefunctions at large or small r. An example of such properties is the generalized oscillator strength near a threshold energy ($\varepsilon = 0$) crucially depends upon the radial wavefunctions at large r, as we shall fully document in Subsection 3.2.

Many properties of the realistic potential V(r) have been extensively studied (Rau and Fano 1968), their consequences to radial wavefunctions P's have been elucidated in great detail (Fano et al 1976, Manson 1976, Manson 1977, Manson 1978, Manson and Dill 1978), especially in connection with the optical oscillator strength spectra, i.e., df(K,E)/dE at the limit $K \to 0$. Calculations by Manson (1972a, 1972b) and their extensions (Manson and Inokuti, 1980) are based on extensive experience with work on the optical oscillator strength. Manson and Inokuti have calculated the spectra of the generalized oscillator strengths for the ionization of the K-shell and the L-shell of all atoms for $Z \leq 30$, but have not published the results comprehensively. In the following section (Section 3.2), some of the results will be discussed.

Leapman et al (1980) and Rez and Leapman (1981) also reported similar calculations on the K-, L-, and M-shell generalized oscillator strengths and related quantities for a selection of atoms, based on virtually the same method as that of Manson and Inokuti. McGuire

(1977, 1979) carried out similar work as well. But his method contains an additional mathematical approximation; he divides the full r-range ($0 < r < \infty$) into several intervals, in each of which the potential V(r) is approximated by a Coulomb potential $-Z_i e^2/r$ with a suitable effective charge number Z_i. This allows one to write down the solution in that interval as a linear combination of regular and irregular Coulomb functions and then to determine the coefficients of the linear combination by requirement of smooth connection of the wavefunctions P's. This procedure may very well be more efficient than the straightforward numerical solution of Eqs. (17) and (21), done by Leapman et al (1980) and by Manson and Inokuti, but has a definite possibility of generating spurious results.

Finally, calculations more accurate than the Hartree-Slater potential field method are indeed possible, for example, by the use of the Hartree-Fock method, the random-phase approximation, or the method of configuration mixing. Yet, as far as the properties of deep inner-shell are concerned, more accurate calculations are unlikely to alter drastically the results of the Hartree-Slater calculations. The reason for this expectation comes from the well-known notion of the perturbation theory; the possible corrections to the Hartree-Slater calculations must arise from the perturbative contributions from virtual excited states, but these states are located at very high excitation energies when one deals with a deep inner-shell state.

3.2 Generalized Oscillator Strengths for Inner Shells of Atoms: Results

The most suitable way to show the data of the generalized oscillator strength is the plot first given by Miller and Platzman (1957). By use

of Eqs. (4), (7), (9), and (10), one can readily see that it is suitable to plot df(K,E)/dE at fixed E as a function of ln (Ka_0). Equivalently, one may plot $Q^{-1}|\eta_E(K)|^2$ as a function of ln Q. Then, the area under the curve represents the integrated cross section over a range of the momentum transfer $\hbar K$ (or over a range of the scattering angle). To show this point precisely, we may rewrite Eq. (7) as

$$d\sigma_E = \frac{8\pi a_0^2 R}{mv^2} \frac{R}{E} \frac{df(K,E)}{dE} d[\ln (Ka_0)^2]. \tag{24}$$

For fixed incident electron speed v and fixed energy loss E, the momentum transfer is uniquely calculable through kinematics. Therefore, the Miller-Platzman plot is a graphical representation of the angular distribution of inelasticially scattered electrons at fixed v and E. Yet, it takes some time and experience for anyone to become fully familiar with the relation between θ and $(Ka_0)^2$. As an aid to this end, we present here Fig. 6, which shows the relation for energy-transfer values corresponding to the K-shell threshold (E = 1.57 keV) and to the 2s-subshell threshold (E = 127 eV) of aluminum. The figure illustrates several points. First, $(Ka_0)^2$ varies over a wide range with varying θ. Second, the range of the variation in $(Ka_0)^2$ becomes greater and greater with increasing incident speed v. Third, $(Ka_0)^2$ depends weakly on θ for sufficiently small θ, but becomes roughly proportional to θ^2 at large θ; the transition between the two kinds of dependence occurs at smaller and smaller θ with increasing v.

Following figures are examples of the Miller-Platzman plot showing the results of calculations by Manson and Inokuti for selected atoms. These

figures also show the corresponding results of the hydrogenic approximation. Mancon and Inokuti have actually calculated and plotted the generalized oscillator-strength density df(K,E)/d(E/R) for the ionization from the 1s, 2s, and 2p orbits of all atoms through Zn (Z = 30). We shall respond to any reasonable request for providing any of the numerical or graphical data we have at hand.

Figures 7-11 concern aluminum. Let us discuss each of them in turn. Figure 7 shows results for the ionization of the 2s-subshell, which has the binding energy B = 127 eV according to Shirley et al (1977). Each curve represents the density df(K,E)/d(E/R) of the generalized oscillator strength per unit range of $E/R = (\varepsilon + B)/R$, where ε is the kinetic energy of an ejected electron. Plot (1) shows results for the lowest ε values, i.e., $\varepsilon/R = 0$, 0.5, 1.0, 1.5, and 2.0. In particular, the solid curves represent Hartree-Slater results, and the chained curves hydrogenic-approximation results. In either case, the curve lying highest at smallest $(Ka_0)^2$ corresponds to $\varepsilon/R = 0$; the curve lying next highest at smallest $(Ka_0)^2$ corresponds to $\varepsilon/R = 0.5$, and so on. In other words, the optical limit df(0,E)/d(E/R) is monotomically decreasing with ε, as is always the case for the hydrogenic-approximation.

Nevertheless, Fig. 7, Plot (1) illustrates a sharp difference of the Hartree-Slater results from the hydrogenic-approximation results. First of all, the magnitude at $(Ka_0)^2 \to 0$ is more than twice the hydrogenic-approximation value at $\varepsilon/R = 0$. Second, the same magnitude stays virtually constant for the range $0.5 \leqq \varepsilon/R \leqq 2.0$, while the hydrogenic-approximation

value decreases steadily with increasing ε/R. Finally, in the same ε range, the Hartree-Slater results show the gradual development of the maximum at a high $(Ka_0)^2$ value, i.e., the emergence of the Bethe ridge.

In Fig. 7, Plot (2), one begins to observe the approach to the hydrogenic behavior. Here, the solid curves represent the Hartree-Slater results for ε/R = 3, 4, 5, 6, and 8, in the order of decreasing height at low $(Ka_0)^2$; the chained curves represent the hydrogenic-approximation results for the same ε/R values also in the order of decreasing height. Throughout the ε range of Plot (2), the Hartree-Slater results indicate the full development of the Bethe ridge. In contrast, the hydrogenic-approximation results begin to show the Bethe ridge only belatedly with increasing ε.

In Fig. 7, Plot (3), one sees the virtual agreement with the hydrogenic-approximation. The curves show results for ε/R = 10, 15, 20, 25, and 30 in the order of decreasing height; this applies to both the Hartree-Slater results (shown by the solid curves) and the hydrogenic-approximation results.

Figure 8 concerns the ionization of the 2p-subshell, which has the binding energy B = 81 eV. Plot (1) shows results for the same set of the lowest ε values, ε/R = 0, 0.5, 1.0, 1.5, and 2.0. The chained curves are based on the hydrogenic-approximation, and show the monotonic decrease of the generalized oscillator strength with increasing ε. By sharp contrast, the Hartree-Slater values (shown by the solid curves) are increasing with increasing ε; the lowest solid curve shows the Hartree-

Slater value for $\varepsilon/R = 0$, which is less than one-tenth the corresponding hydrogenic-approximation value. Plot (2) shows results for $\varepsilon/R = 3$, 4, 5, 6, and 8. Both the Hartree-Slater results (shown by the solid curves) and the hydrogenic-approximation results (shown by the chained curves) are decreasing with increasing ε. Plot (3) shows the close approach to the hydrogenic behavior, realized for $\varepsilon/R = 10$, 15, 20, 25, and 30; the highest curve corresponds to $\varepsilon/R = 10$, the next highest to $\varepsilon/R = 15$, and so on.

The peculiar behavior of the 2p-generalized oscillator strength at low ε and low K, in sharp disagreement from the hydrogenic-approximation results, is attributable to the phenomenon of the delayed maximum in photoabsorption cross sections.

Detailed interpretation of the delayed maximum in the 2p ionization of aluminum was given by Manson (1972b). Briefly, this arises from the ε-dependence of the d-continuum final state, which is the dominant contributor to the generalized oscillator strength. [See Fig. 3 of Manson (1972b)]. At $\varepsilon/R = 0$ and small ε/R, the centrifugal potential keeps the d-continuum wave out of small distances at which the initial 2p wavefunction has appreciable magnitudes, and therefore the radial matrix element [Eq. (16)] must become small. At higher ε/R, the d-continuum wave begins to reach the small distances and to attain appreciable overlap with the initial 2p state. According to Eq. (21), the total effective potential

$$U(r) = V(r) - \hbar^2 \ell(\ell + 1)/2mr^2 \qquad (25)$$

with $\ell = 2$ determines the d wave. As Fig. 9 shows, U(r) gives rise to a

shallow, but wide-ranged attractive region. As a result, properties of the d-wave changes markedly between $\varepsilon/R = 0$ and $\varepsilon/R = 2.0$ (see Fig. 10). For example, the phase shift δ (with respect to the Coulomb wave) increases considerably with ε. [See Fig. 3 of Manson (1969).] The change of δ here is only about 0.7 radians, and the situation is different from a typical resonance which is associated with a change of δ by almost π and implies the presence of a quasi-bound state. Nevertheless there is significant ε-dependence of some d-wave properties, most notably the d-wave amplitude, which is defined as follows. According to Eq. (21), the continuum wavefunction $P_{\varepsilon\ell}(r)$ behaves near $r = 0$ as

$$P_{\varepsilon\ell}(r) = C_{\varepsilon\ell}\, r^{\ell+1}, \tag{26}$$

where $C_{\varepsilon\ell}$ is a number, depending on ε and ℓ, to be determined so that the normalization relation, Eq. (22), is satisfied. The determination requires knowledge of the unnormalized wavefunction over the entire r domain. Analysis shows that $|C_{\varepsilon\ell}|^2$ is the major factor that determines the ε-dependence of the matrix element over a small ε interval. It should be also noted that $|C_{\varepsilon\ell}|^2$ is virtually the same as the notion of the density of states, often used by solid-state theorists.

Figure 11 shows results for the ionization of the K-shell (1s shell) of aluminum. For simplicity, we include here results for two values of ejected-electron energy, i.e., $\varepsilon/R = 0$ and $\varepsilon/R = 0.5$. The hydrogenic-approximation results (shown in the chained curves) are decreasing with ε: the upper curve refers to $\varepsilon/R = 0$, and the lower one to $\varepsilon/R = 0.5$. The

Hartree-Slater results (shown in the solid curves) are opposite in the order: the lower curve refers to $\varepsilon/R = 0$, and the upper one to $\varepsilon/R = 0.5$. Here again, the non-monotonic behavior in ε is attributable to that of $|C_{\varepsilon\ell}|^2$.

Before concluding this Subsection, we point out the generality of many observations we made above. First of all, the non-hydrogenic behavior of the generalized oscillator is seen in all atoms we studied, whenever the kinetic energy ε of an ejected electron is small or comparable to the atomic potential in the relevant spatial region. Second, the delayed maximum is common to many instances of $p \rightarrow d$ transitions, where the final d-wave is governed by the effective potential U having a well-and-hump structure. Actually, the case of d-waves for aluminum is not the most clearcut. The d-wave potential for chlorine, argon, or potassium shows a much more pronounced hump, and the delayed maximum is much more prominent (see Fig. 12). Third, the near-threshold structure of the kind we saw in the K-shell ionization of aluminum is common to all the atom (Manson and Inokuti 1980, and Holland et al 1978). To illustrate the common occurence of the non-hydrogenic behavior, we present Figs. 13-15, which show selected results.

We should also note that there are many other ways for showing data than the Miller-Platzman plot (which is the most fundamental). For instance, one could show the generalized oscillator strength as a function of ε, either at fixed K or at fixed θ. We may call the result a spectral plot. Figure 16 is an example. A spectral plot of the differential

cross section $d\sigma_E/d\omega$ at a fixed θ is often called an electron energy loss spectrum. Often one sees in the literature an energy loss spectrum of a slightly different kind, i.e.,

$$\Delta\delta_E = \int_0^{\hat{\theta}} (d\sigma_E/d\omega)\ d\omega\ , \tag{27}$$

plotted as a function of E, for a fixed apperture angle. Inokuti (1978) gave some general remarks on this quantity. Leapman et al (1980) and Rez and Leapman (1981) have presented extensive results on this quantity of frequent reference in electron microscopy.

3.3 Molecular and Solid-State Effects

In many instances we have seen much evidence for the role of atomic fields in governing the motion of an ejected electron, especially when its energy is low. For a molecule, the field of force seen by an ejected electron is in general nonspherical because of the molecular geometry. This is so even though the electronic structure of deep inner shells is affected only modestly by the molecular binding, as seen by the chemical shifts of core binding energies [See Shirley et al (1977) and Carlson (1975).]

Molecular effects on the optical oscillator strength, i.e., $df(K,E)/dE$ at $K \to 0$, have been recognized both experimentally and theoretically, and much of the understanding here should be pertinent to the generalized oscillator strength at finite momentum transfer. (However, there has been no extensive calculation specifically for molecules.)

Figure 17 illustrates a dramatic example of molecular effects. This figure shows the photoionization cross section (the same as $df(K,E)/dE$

at K → 0, apart from a universal constant) for the K-shell of molecular nitrogen, as calculated by Dehmer and Dill (1976). The calculation is based upon a single-electron picture (like the calculation on atoms we saw in Subsections 3.1 and 3.2), and upon a potential that is manifestly non-spherical. Because of the molecular geometry, one must distinguish four final-state classes designated by symbols σ_g, σ_u, π_g, and π_u, as opposed to the single class (the p state) for an atom. Whereas three of the classes show a smooth behavior for lower energies ε of ejected electrons, the σ_u symmetry gives rise to a sharp peak at about $\varepsilon/R = 1.2$, and causes a marked difference from the atomic case. According to Dehmer and Dill (1976), the origin of the peak is a shape resonance, i.e., the appearance of a quasi-bound state in the molecular potential field. Roughly speaking, an electron in the σ_u state at that energy is temporarily trapped by the field before escaping out eventually. The shape resonance is a general occurence for many molecules. Indeed, a review article by Dehmer and Dill (1979) shows many other examples.

In solid-state contexts, effects analogous to the shape resonance are often called XANES (x-ray absorption near-edge structure), and have been the subject of many recent studies. Examples of theoretical studies include Durham et al (1981) and Durham et al (1982).

One sees another feature that distinguishes the molecule from the atom. That is to say, there are undulations at higher energies $\varepsilon \geq 10$ R in all the four symmetry classes. These undulations were recognized much earlier, and are known as EXAFS (extended x-ray absorption fine structures) [See Teo and Joy (1981) for example.] Briefly, the undula-

tions result from constructive and destructive interference of ejected-electron waves with those scattered from different atoms. The variation with energy is roughly represented by $\sin(kD)$, where $k = (\varepsilon/R)^{\frac{1}{2}}/a_0$ is the wave number of the ejected electron and D is the internuclear distance. Because of the origin, it is easy to see that the EXAFS is in principle universal to all molecules and solids, even though the size of the undulations is often small and the pattern is more complicated for cases involving many and different atoms. Indeed the notion of the EXAFS is so well-known and prevailing in solid-state physics that Holland et al (1978) adapted an EXAFS theory to interpret the near-threshold structure of atomic K-shell spectra.

The shape resonance and the EXAFS are two well recognized molecular effects. In reality, there are further effects contributing to the near-edge structure of inner-shell spectra of molecules and solids. Indeed, the electron energy loss spectrum obtained experimentally by Wight et al (1973), shown as Fig. 18, indicates peaks additional to the shape-resonance peak. [Note that the energy loss spectrum in the forward scattering is roughly $E^{-3}\, df(K,E)/dE$, plotted as a function of E and is thus distorted from the optical oscillator-strength spectrum. See Sec. 3.1 of Inokuti (1971).] Some of the additional peaks are attributed to effects beyond the single-electron picture, e.g., simultaneous excitation of another electron with the inner-shell ionization.

In conclusion, we may reiterate that there has been no calculation of the generalized oscillator strength of inner shells <u>specifically including molecular or solid-state effects.</u> Yet, the developments

described above suggest that there is already enough groundwork for such a calculation, in both concepts and techniques and that the time may be ripe for a major undertaking.

ACKNOWLEDGMENTS

We thank C. E. Brion, J. L. Dehmer, J. Geiger, and H. F. Wellenstein for their generous permission and assistance for reproducing here figures or data from their publications.

REFERENCES

1. Barlas, A. D., W. Ruekner, H. F. Wellenstein (1977). High energy electron impact spectroscopy measurement on the Compton effect. Phil. Mag. 36, 201-207.

2. Bethe, H. (1930). Zur Theorie des Durchgangs schneller Korpuskularstrahlen durch Materie. Ann. Phys. (Leibzig) 5, 325-400.

3. Bethe, H. (1932). Bremsformel für Elektronen relativischer Geschwindigkeiten. Phys. 76, 293-299.

4. Bethe, H. (1933). Quantenmechanik der Ein- und Zwei-Elektronenprobleme. Chapter 3 in Handbuch der Physik, edited by H. Geiger and K. Scheel, Vol. 24/1, pp. 273-560. Verlag von Julius Springer, Berlin.

5. Bohr, N. (1948). The penetration of atomic particles through matter. K. Dan. Videns. Selsk., Mat. Fys. Medd. 18, No. 8, 1-144.

6. Bonham, R. A. and H. F. Wellenstein (1973). Measurements of quantities related to the charge and momentum densities of atoms and molecules by use of keV electron scattering. Int. J. Quantum Chem. Symp. No. 7, 377-394.

7. Carlson, T. A. (1975). Photoelectron and Auger Spectroscopy, Plenum Press, New York.

8. Dehmer, J. L. and D. Dill (1977). Molecular effects on the inner-shell photoabsorption. K-shell spectrum of N_2. J. Chem. Phys. 65, 5327-5334.

9. Dehmer, J. L. and D. Dill (1979). The continuum multiple-scattering approach to electron-molecule scattering and molecular photoionization. in Electron-Molecule and Photon-Molecule Collisions, edited by T. Rescigno, V. McKoy, and B. Schneider (Plenum Press, New York) pp. 225-265.

10. Durham, P. J., J. B. Pendry, and C. H. Hodges (1981). XANES: Determination of bond angles and multi-atom correlations in order and disordered systems. Solid State Commun. 38, 159-162.

11. Durham, P. J., J. B. Pendry, and C. H. Hodges (1982). Calculation of x-ray absorption near-edge structure. Comput. Phys. Comm., in press.

12. Fano, U. (1956). Atomic theory of electro-magnetic interactions in dense materials. Phys. Rev. 103, 1202-1218.

12. Fano, U. and J. W. Cooper (1968). Spectral distribution of atomic oscillator strength. Rev. Mod. Phys. 40, 441-507.

13. Fano, U., Theodosiou, and J. L. Dehmer (1976). Electron-optical properties of atomic fields. Rev. Mod. Phys. 48, 49-68.

14. Fermi, E. (1940). The ionization loss of energy in gases and condensed materials. Phys. Rev. 57, 485-493.

15. Ferrell, R. A. (1957). Characteristic energy loss of electrons passing through metal foils: dispersion relation and short wavelength cutoff for plasma oscillations. Phys. Rev. 107, 450-462.

16. Geiger, J. (1964). Streuung von 25 keV-Elektronen an Gasen. II. Streuung an Neon, Argon, Krypton und Xenon. Z. Phys. 177, 138-145.

17. Holland, B. W., J. B. Pendry, R. F. Pettifer, and Bordas (1978). Atomic origin of structure in EXAFS experiments. J. Phys. C 11, 633-642.

18. Inokuti, M. (1971). Inelastic collisions of fast charged particles with atoms and molecules - The Bethe theory revisited. Rev. Mod. Phys. 43, 297-347.

19. Inokuti, M. (1978). Electron-scattering cross sections pertinent to electron microscopy. Ultramicroscopy 3, 423-427.

20. Inokuti, M., J. L. Dehmer, T. Baer, and J. D. Hanson (1981). Oscillator-strength moments, stopping powers, and total inelastic-scattering cross sections of all atoms through strontium. Phys. Rev. A 23, 95-109.

21. Inokuti, M., Y. Itikawa, and J. E. Turner (1978). Addenda: Inelastic collisions of fast charged particles with atoms and molecules -- The Bethe theory revisited. [Rev. Mod. Phys. 43, 297 (1971)]. Rev. Mod. Phys. 50, 23-35.

22. Inokuti, M., Y.-K. Kim, and R. L. Platzman (1967). Total cross sections for inelastic scattering of charged particles by atoms and molecules. I. A sum rule for the Bethe cross sections and its application to the helium atom. Phys. Rev. 164, 55-61.

23. Khandelwal, G. S. and E. Merzbacher (1966). Stopping power of M electrons. Phys. Rev. 144, 349-352.

24. Lahmam-Bennani, A., A. Duguet, and H. F. Wellenstein (1979). Bethe surface and Compton profile for CO_2 obtained by use of 35-keV incident electrons. Chem. Phys. Lett. 60, 405-410.

25. Lahmam-Bennani, A., A. Duguet, H. F. Wellenstein, and M. Ronault (1980). Bethe surface and Compton profile of NH_3 obtained by 35-keV electron impact. J. Chem. Phys. 72, 6398-6408.

26. Landau, L. D. and E. M. Lifshitz (1960). Electrodynamics of Continuous Media, translated by J. B. Sykes and J. S. Bell, Pergamon, London. See Chapters IX and XII in particular.

27. Lassettre, E. N., A. Skerbele, and M. A. Dillon (1969). Generalized oscillator strength for $1^1S \rightarrow 2^1P$ transition of helium. Theory of limiting oscillator strength. J. Chem. Phys. 50, 1829-1839.

28. Leapman, R. D., P. Rez, and D. F. Mayers (1980). K-, L-, and M-shell generalized oscillator strengths and ionization cross sections for fast electron collisions. J. Chem. Phys. 72, 1232-1243.

29. Manson, S. T. (1969). Dependence of the phase shift on energy and atomic number for electron scattering by atomic fields. Phys. Rev. 182, 97-103.

30. Manson, S. T. (1972a). Theoretical study of generalized oscillator strengths in atoms: Comparison with experiment and other calculations. Phys. Rev. A 5, 668-677.

31. Manson, S. T. (1972b). Inelastic collisions of fast charged particles with atoms: Ionization of the aluminum L-shell. Phys. Rev. A 6, 1013-1024.

32. Manson, S. T. (1976). Atomic photoelectron spectroscopy, Part I. in Advances in Electronics and Electron Physics, edited by L. Marton, Academic Press, New York, Vol. 41, pp. 73-111.

33. Manson, S. T. (1977). Atomic photoelectron spectroscopy, Part II. in Advances in Electronics and Electron Physics, edited by L. Martin, Academic Press, New York, Vol. 44, pp. 1-32.

34. Manson, S. T. (1978). The calculation of photoionization cross sections; An atomic view. in Topics in Applied Physics, Vol. 26, Photoemission in Solids, I. General Principles, edited by M. Cardona and L. Ley, Springer-Verlag, Berlin. pp. 135-163.

35. Manson, S. T. and D. Dill (1978). The photoionization of atoms: Cross sections and photoelectron angular distributions. in Electron Spectroscopy, Theory, Techniques, and Applications, edited by C. R. Brundle and A. D. Baker, Academic Press, New York, Vol. 2, pp. 157-195.

36. Manson, S. T. and M. Inokuti (1980). Near-threshold structure in the atomic K-shell spectra for ionization by photons or fast charged particles. J. Phys. B 13, L323-L326.

37. Matsuzawa, M., Mitsuoka, and M. Inokuti, (1979). Integrals of the squared atomic form factor over the momentum transfer. J. Phys. B 12, 3033-3046.

38. McCarthy, I. E. and E. Weigold (1976). (e,2e) Spectroscopy. Phys. Rep. 27, 275-371.

39. McGuire, E. J. (1977). Scaled electron ionization cross sections in the Born approximation. Phys. Rev. A 16, 73-79.

40. McGuire, E. J. (1979). Scaled electron ionization cross sections in the Born approximation for atoms with $55 \leq Z \leq 102$. Phys. Rev. A 20, 445-456.

41. Miller, W. F. and R. L. Platzman (1957). On the theory of the inelastic scattering of electrons by helium atoms. Proc. Phys. Soc. (London) 70, 299-303.

42. Nozières, P. and D. Pines (1959). Electron interaction in solids. Characteristic energy loss spectrum. Phys. Rev. 113, 1254-1267.

43. Powell, J. C. (1982). Inelastic scattering of electrons in solids. Proceedings of the present conference.

44. Raether, H. (1980). Excitation of Plasmons and Interband Transitions by Electrons. Springer-Verlag, Berlin.

45. Rau, A.R.P. and U. Fano (1968). Atomic potential wells and the periodic table. Phys. Rev. 167, 7-10.

46. Rez. P. and R. D. Leapman (1981). Core loss shape and cross section calculations. in Analytical Electron Microscopy - 1981, edited by R. H. Geiss (San Francisco Press, San Francisco), pp. 181-186.

47. Shiles, E., T. Sasaki, M. Inokuti, and D. Y. Smith (1980). Self-consistency and sum-rule tests in the Kramers-Kronig analysis of optical data: Applications to aluminum. Phys. Rev. B 22, 1612-1628.

48. Shirley, D. A., R. L. Martin, S. P. Kowalczyk, F. R. McFeely, and L. Ley (1977). Core-electron binding energies of the first thirty elements. Phys. Rev. B 15, 544-552.

49. Teo, B. K. and C. Joy (eds.) (1981). EXAFS Spectroscopy, (Plenum Press, New York).

50. Walske, M. C. (1952). The stopping power of K-electrons. Phys. Rev. 88, 1283-1289.

51. Walske, M. C. (1956). Stopping power of L-electrons. Phys. Rev. 101, 940-944.

52. Wight, G. R., C. E. Brion, and M. J. van der Wiel (1972). K-shell energy loss spectra of 2.5 keV electrons in N_2 and CO. J. Electron Spectrosc. Rel. Penom. 1, 457-469.

53. Wong, T. C., J. S. Lee, H. F. Wellenstein, and R. A. Bonham (1975). Experimental definition of valence shell and cumulative-shell Compton profiles from 25-keV electron-impact studies on N_2, Ne, and Ar. Phys. Rev. A 12, 1846-1858.

Captions for Figures

Fig. 1. Differential cross sections for collisions of 25-keV electrons with a neon atom.

The horizontal axis represents the common logarithm of the scattering angle θ. The vertical axis represents the logarithm of the cross section per unit solid angle $d\sigma/d\omega$ measured in the squared Bohr radius $a_0^2 = 0.280 \times 10^{-16}$ cm^2. The curve labeled "elastic" shows the elastic-scattering cross section. The curve labeled E = 16.9 eV represents the cross section for the excitation to the $2p^5 3s$ state. The curve labeled E = 20 eV represents the cross section for the excitation to $2p^5 4s$ and all higher states combined. All the above are based on data given by Geiger (1964). The curve labeled "K-shell ionization" is based on the theoretical generalized oscillator strength calculated by the present authors. The broken straight lines are drawn to show the θ^{-2}-dependence of the cross sections, valid at a range of intermediate θ values.

Fig. 2. The Bethe surface for atomic hydrogen.

The horizontal axes for E/R and ln $(Ka_0)^2$ define the base plane. The vertical axis represents Rdf(K,E)/dE. The fourteen plates are placed at E/R = 3/4, 8/9, 1, 5/4, 3/2, 2, 3, 4, 5, 6, 7, 8, 9, and 10. The broken curve on the base plane shows the location $(E/R) = (Ka_0)^2$ of the Bethe ridge, which is the main feature for $E/R \gg 1$; collisions represented by a point near the Bethe ridge occur as though the incident particle were to strike a free electron, the electron binding being of secondary importance. The optical region $(Ka_0)^2 \ll 1$ is

conspicuous only for small E/R. View (a) shows the gradual spreading of the Bethe ridge with decreasing E/R, and eventually its merger with the optical plateau at the region of small $(Ka_0)^2$ and E/R. View (b) shows in front a cut at $\ln (Ka_0)^2 = -4$, i.e., a curve that closely approximates the photoabsorption cross section. This figure is taken from Inokuti (1971).

Fig. 3. The Bethe surfaces of carbon dioxide and ammonia, after Lahmam-Bennani et al (1979, 1980), reproduced with permission by the authors and the publishers.

The base plane is defined by E/R (the energy transfer measured in the Rydberg energy, 13.6 eV) and by $\ln (Ka_0)^2$ (in the notation of the present article). The dashed curve indicates the Bethe ridge for valence electrons. Notice the K-shell ionization contributions near the threshold energies of carbon, nitrogen and oxygen atoms.

Fig. 4. The total inelastic-scattering cross section σ_{tot} (measured in $\mathring{A}^2$) for 50-keV electrons, plotted against atomic number Z.

The solid line shows the result of calculations that incorporates relativistic kinematics for the incident electron. For comparison, the dotted line shows the results of calculations that disregard relativistic kinematics. The figure is taken from Inokuti et al (1981).

Fig. 5. The mean energy transfer E_{Av} per inelastic collision (measured in eV) for 50-keV electrons, plotted against atomic number Z.

The general features of the curve are the same for all charged particles incident with sufficiently high speed. The dotted line shows the limiting E_{Av} for any extremely relativistic particle. The figure is taken from Inokuti et al (1981).

Fig. 6. The relation between θ and $(Ka_0)^2$.

Suppose that the incident electron has kinetic energy T and momentum p, then $T + mc^2 = [(cp)^2 + (mc^2)^2]^{\frac{1}{2}}$. Suppose that the scattered electron has kinetic energy T' and momentum p', then $T' + mc^2 = [(cp')^2 + (mc^2)^2]^{\frac{1}{2}}$. The energy loss E is defined by $T' = T - E$. The squared momentum transfer is given by $(K\hbar)^2 = p^2 + p'^2 - 2pp' \cos\theta$. These relations enable one to calculate $(Ka_0)^2$ for a given set of T, E, and θ. Here we show $\log_{10} (Ka_0)^2$ as a function of $\log_{10}\theta$, for fixed T and E. Part (a) shows the relation for E = 1.57 keV, corresponding to the threshold for K-shell ionization of aluminum. Part (b) shows the same relation for E = 127 eV, corresponding to the threshold for the 2s-subshell ionization of aluminum. In each case, five curves refer to different kinetic energies T of the incident electron: 10 keV (————), 50 keV (------), 100 keV (— - — -), 500 keV (— · — ·), and 1 MeV (—— - —— -). For the lowest T (10 keV), the curve for each E starts highest at small θ and ends lowest at large θ. For higher and higher T, the curve covers wider and wider ranges. Comparison of Part (a) and Part (b) readily indicates that, for fixed T and for the same θ interval, the range of $(Ka_0)^2$ values is wider for smaller E [i.e., in Part (b).].

Fig. 7. The generalized oscillator strength for the ionization of the 2s-subshell of aluminum.

The horizontal axis represents $\ln (Ka_0)^2$ and the vertical axis represents the density $df(K,E)/d(E/R)$ of the generalized oscillator strength per unit range of $E/R = (\varepsilon + B)/R$, where ε is the kinetic

energy of an ejected electron, and B is the binding energy of the shell, or the threshold for the ionization from that shell. In this case, B = 127 eV, according to Shirley et al (1977). Plot (1) shows values for ε/R = 0, 0.5, 1.0, 1.5, 2.0. Plot (2) shows values for ε/R = 3, 4, 5, 6, 8. Plot (3) shows values for ε/R = 10, 15, 20, 25, 30. The three sets of ε/R values are standard and common to many of the figures to follow. In all plots (including the figures to follow), the solid curves represent Hartree-Slater results, and the chained curves hydrogenic-approximation results. In Plot (1), the curve lying highest at the smallest ln $(Ka_0)^2$ values corresponds to ε/R = 0, the curve lying next highest at the smallest ln $(Ka_0)^2$ values to ε/R = 0.5, and so forth.

Fig. 8 The generalized oscillator strength for the ionization of the 2p-subshell of aluminum.

The threshold energy B is 81 eV according to Shirley et al (1977). The standard sets of ε/R values are used for Plot (1), Plot (2), and Plot (3). Most of the captions to Fig. 7 apply here. As an exception, in Plot (1) only, the Hartree-Slater results (shown by solid curves) are increasing with increasing ε; in other words, the lowest-lying solid curve corresponds to ε/R = 0, the next lowest curve to ε/R = 0.5, and so forth.

Fig. 9 The total effective potential for a d electron (ℓ = 2) emerging from the aluminum atom.

The potential U is defined by Eq. (25) of the text, and its value measured in R is here plotted against distance r measured in a_0.

Plot (1) shows the Hartree-Slater potential over the wide range of r. Note the hump around $r/a_0 = 3.3$. Even though the top of the hump is below zero energy, the potential gives rise to the marked difference in the behavior of the radial functions for $\varepsilon/R = 0$ and $\varepsilon/R = 2$, shown in Fig. 10. Plot (2) shows the Hartree-Slater potential (plotted as the solid curve) at small r. It also shows the potential used in the hydrogenic-approximation (plotted as the chained curve). Note the logarithmic vertical scale. The two potentials are similar in the small region $r/a_0 < 0.3$ (except at the close vicinity of the nucleus not shown here), but differ greatly for large r; in particular, the hydrogenic potential stays positive throughout, and approach $V_0/R = 6.82$ [See Eq. (23).]

Fig. 10 Radial wavefunctions for the 2p state and the d-continuum states for aluminum.

The chained-dot curve (— · — ·) shows the d-continuum wavefunction for $\varepsilon/R = 0$, and the chained-dash curve (—— - —— -) the same for $\varepsilon/R = 2$. The plotted values correspond to $\pi^{-\frac{1}{2}} P_{\varepsilon\ell}(r)$ with $\ell = 2$ in the notation of the text. The solid curve shows the normalized 2p bound-state. Notice that the d-continuum wavefunction for $\varepsilon/R = 2$ has a much greater overlap with the 2p state than for $\varepsilon/R = 0$.

Fig. 11 The generalized oscillator strength for the ionization of the 1s-shell (or K-shell) of aluminum.

The threshold energy B is 1.57 keV, according to Shirley et al (1977). Most of the captions to Fig. 7 apply here. An exception is Plot (1). In a deviation from the standard set, we

show here results for $\varepsilon/R = 0$ and $\varepsilon/R = 0.5$ only. The Hartree-Slater results are shown by solid curves; the lower one corresponds to $\varepsilon/R = 0$ and the upper one to $\varepsilon = 0.5$. The hydrogenic-approximation results are shown by chained curves; the upper one corresponds to $\varepsilon/R = 0$, and the lower one to $\varepsilon/R = 0.5$. Another exception is Plot (2), in which the upper curves (both solid and chained) correspond to $\varepsilon/R = 3$ and the lower curves to $\varepsilon/R = 8$, other curves being removed.

Fig. 12 The total effective potential for a d electron emerging from the chlorine atom.

The potential U is defined by Eq. (25) of the text, and its value measured in R is plotted against distance r measured in a_0. The hump around $r/a_0 = 2.5$ stands out to positive energy, and causes a prominent delayed maximum for the 2p → d transition.

Fig. 13 The generalized oscillator strength for the 2p-subshell of chlorine.

The threshold energy B is 210 eV according to Shirley et al (1977). The standard set of the five lowest ε values ($\varepsilon/R = 0$, 0.5, 1, 1.5, 2) is used. The Hartree-Slater results (shown as solid curves) are much lower than the hydrogenic-approximation results (shown as the chained curves), owing to the effects of the effective potential for the d-continuum final states (shown in Fig. 12). Indeed, the Hartree-Slater results are lowest for $\varepsilon/R = 0$, highest for 0.5, and then decreasing for larger ε/R, while the hydrogenic-approximation results are decreasing steadily with increasing ε.

Fig. 14 The generalized oscillator strength for the 2s-subshell of chlorine.

The threshold energy B is 278 eV according to Shirley et al (1977). The standard set of the lowest ε values (ε/R = 0, 0.5, 1, 1.5, 2) is used. The Hartree-Slater results (shown as the solid curves) are increasing with increasing ε, and indicate the emergence of the Bethe ridge, while the hydrogenic-approximation results (shown as the chained curves) indicate no sign of it.

Fig. 15 The generalized oscillator strength for the 2s-subshell of sodium.

The binding energy B is 71 eV according to Shirley et al (1977). Plot (1) shows results for the five lowest ε/R values of the standard set. The Hartree-Slater results (shown as solid curves) are decreasing with increasing ε, while the hydrogenic-approximation results are decreasing with increasing ε. Plot (2) shows the results for the five intermediate ε/R values of the standard set.

Fig. 16 The generalized oscillator strength for the 2p-subshell of sodium, plotted as a function of ejected electron energy at fixed momentum transfer.

Basically the same data shown in Fig. 15 are plotted, <u>but in a different way</u>. The horizontal axis here represents ε/R, i.e., the ejected-electron energy measured in R, at a fixed value of $(Ka_0)^2$. In all cases, the solid curve shows the Hartree-Slater results, and the chained curve the hydrogenic-approximation results. Plot (1) represents $(Ka_0)^2 = 10^{-4}$, i.e., at the optical limit. Plot (2) represents $(Ka_0)^2 = 4$, showing an approach to the hydrogenic-approximation results and the emergence of the Bethe ridge.

Fig. 17 Photoionization cross section of the K-shell of molecular nitrogen.

The figure is reproduced here with permission from Dehmer and Dill (1976). The horizontal axis represents the kinetic energy of an ejected electron measured in Rydbergs, and corresponds to ε/R in the text of the present paper. The vertical axis represents the photoionization cross section σ_{TOT} measured in Mb = 10^{-16} cm^2, which is related to the density of the optical oscillator strength by $\sigma_{TOT} = 4\pi^2(e^2/\hbar c)\, a_0^2\, df(0,E)/d(E/R) = 8.067 \times df(0,E)/d(E/R) \times 10^{-16}$ cm^2. Each of the solid curves shows contributions from the indicated class of final-state symmetry. The dashed curve shows twice the photoionization cross section of the K-shell of atomic nitrogen.

Fig. 18 Electron energy-loss spectrum of molecular nitrogen in the neighborhood of the K-shell threshold (409.9 eV).

The figure is reproduced here with permission from Wight et al (1973). The vertical axis represents the intensity of electrons scattered into the forward direction, the incident energy being 2.5 keV. The strongest peak (labeled as A) corresponds to the shape resonance discussed by Dehmer and Dill (1976).

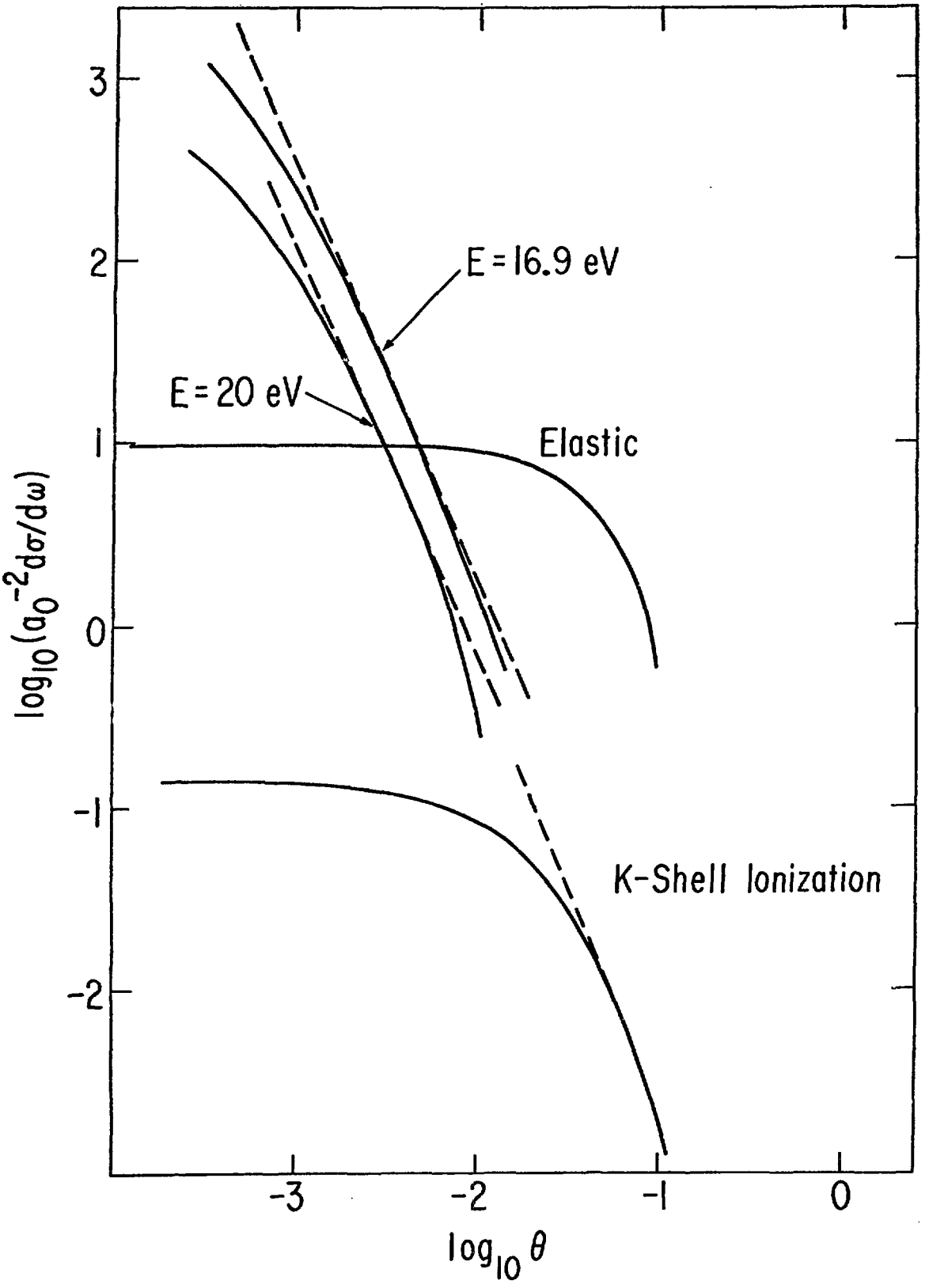
E = 16.9 eV
E = 20 eV
Elastic
K-Shell Ionization
3
2
1
0
-1
-2
-3
-2
-1
0
$\log_{10}(a_0^{-2} d\sigma/d\omega)$
$\log_{10}\theta$

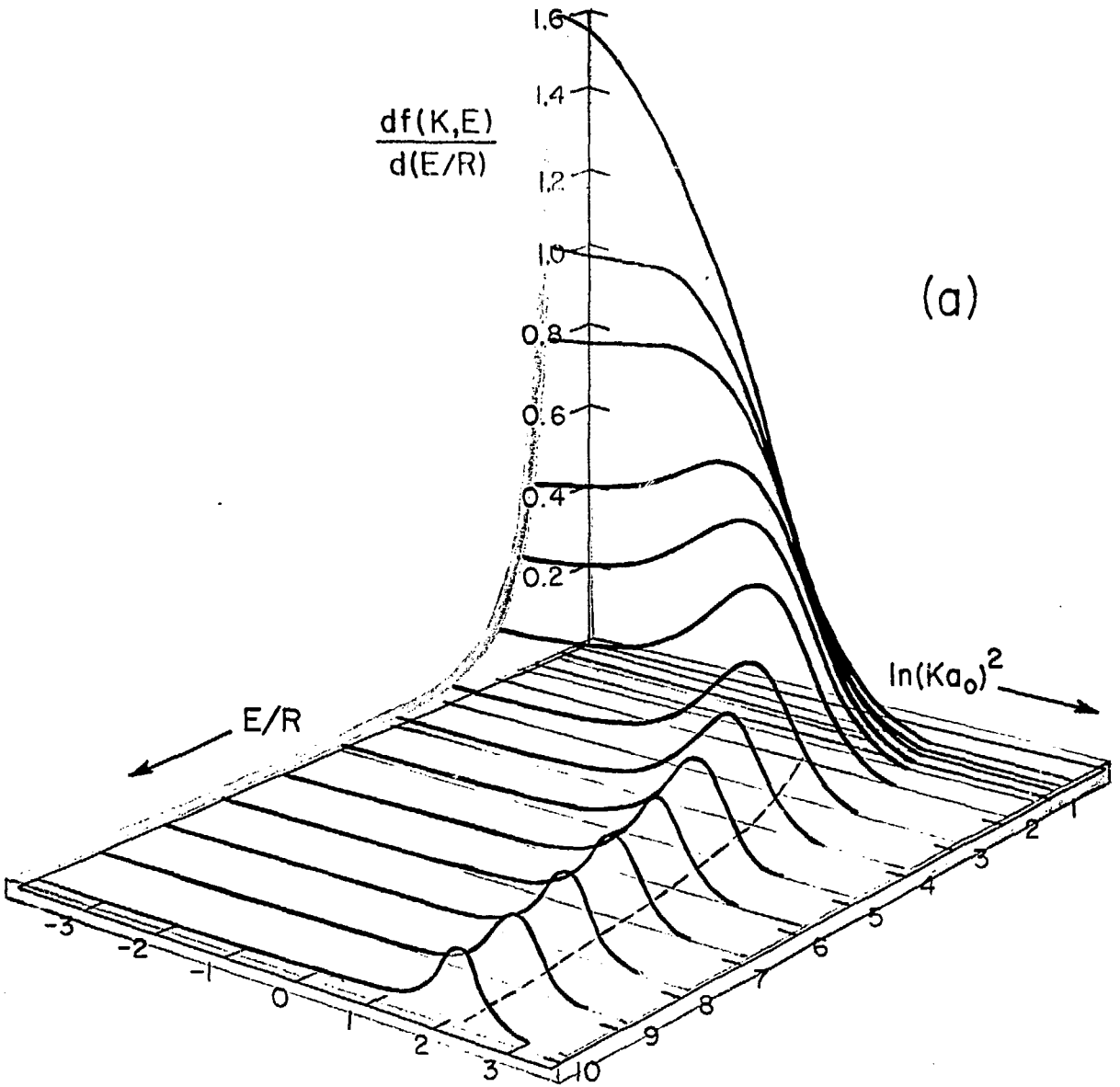
df(K,E)
d(E/R)
1.6
1.4
1.2
1.0
0.8
0.6
0.4
0.2
(a)
E/R
-3
-2
-1
0
1
2
3
ln(Ka0)2
1
2
3
4
5
6
7
8
9
10

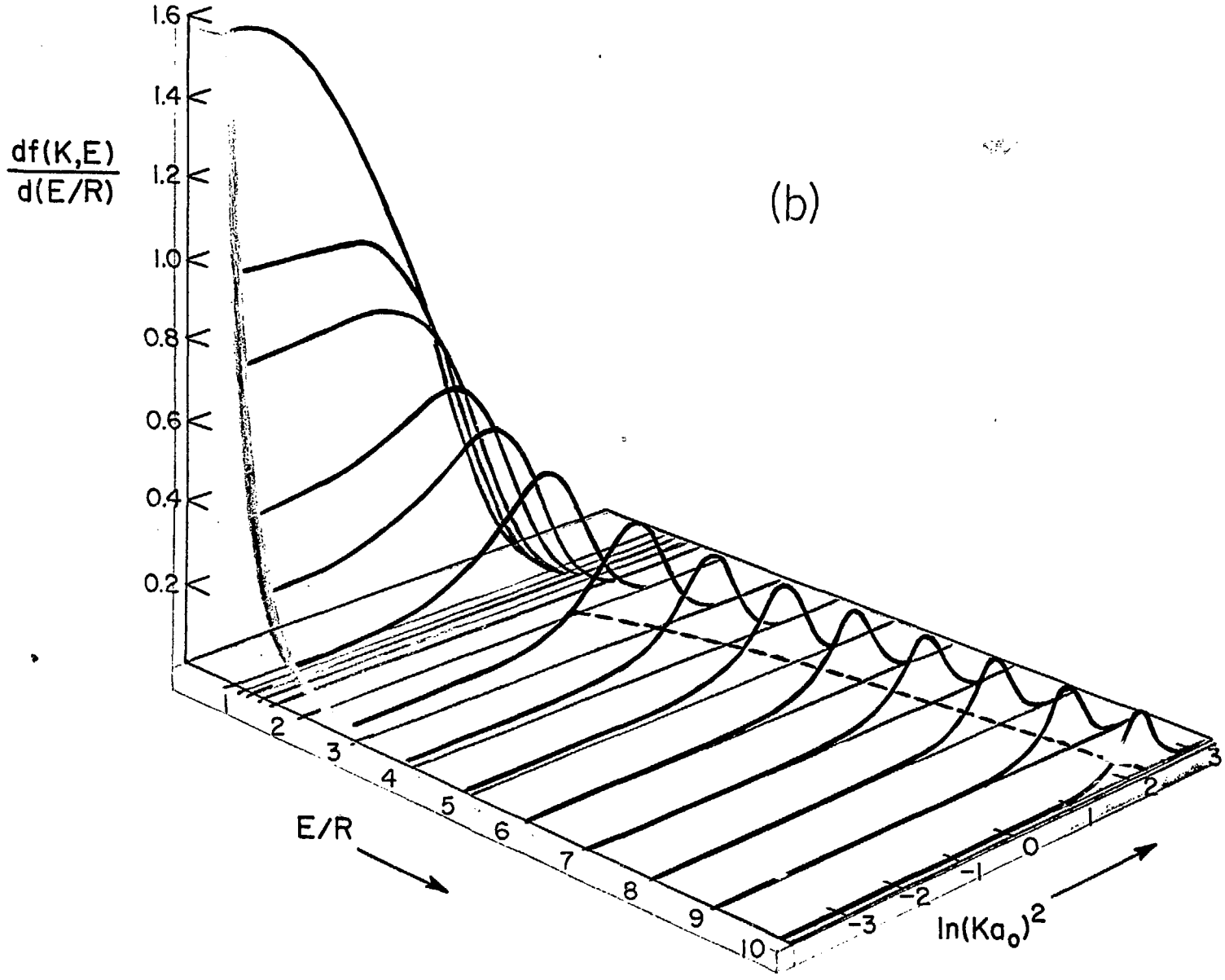
df(K,E)
d(E/R)
1.6
1.4
1.2
1.0
0.8
0.6
0.4
0.2
(b)
1
2
3
4
5
6
7
8
9
10
E/R
-3
-2
-1
0
1
2
3
ln(Ka0)2

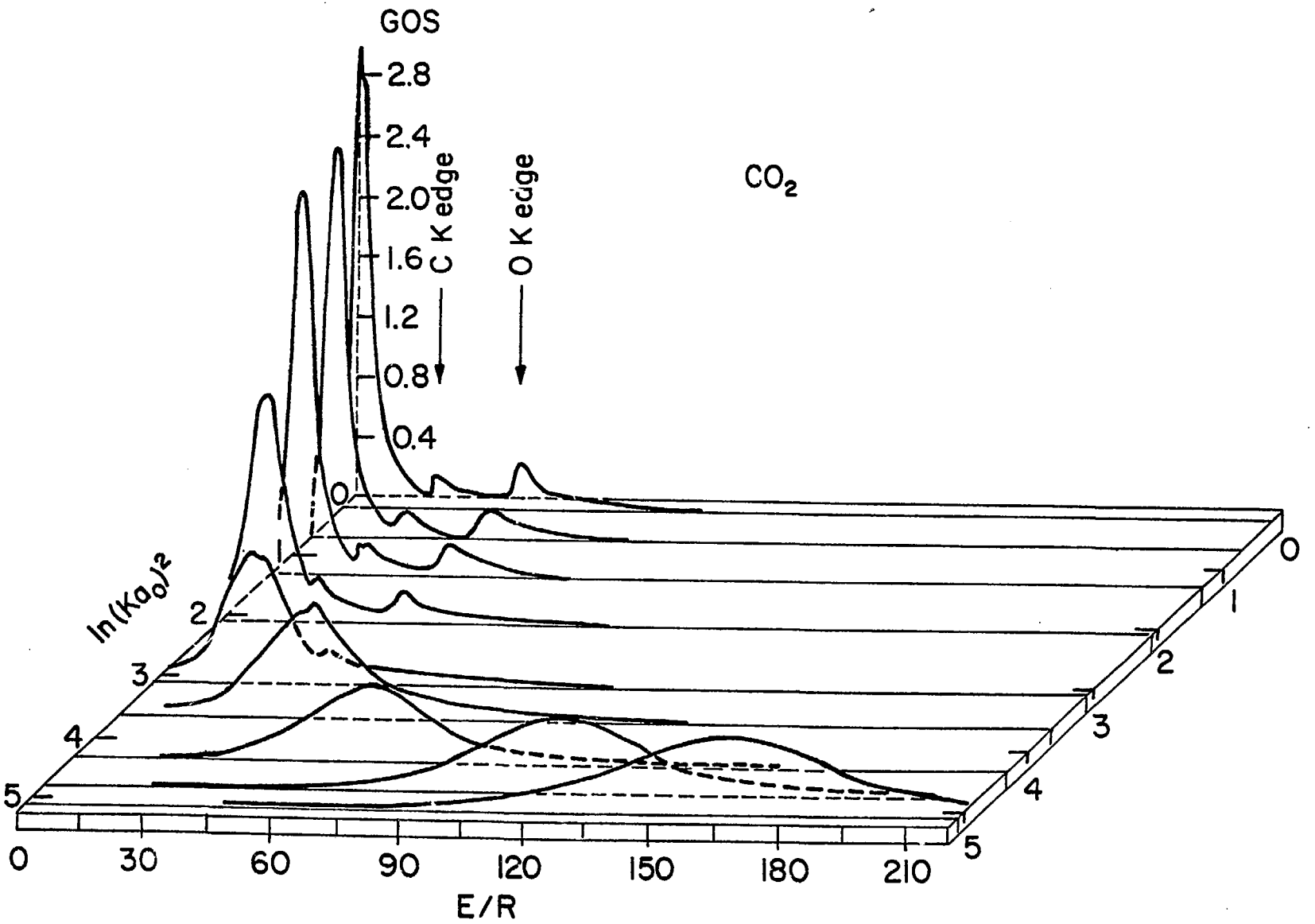
GOS
2.8
2.4
2.0
1.6
1.2
0.8
0.4
C K edge
O K edge
CO_2
$\ln(K_0/)^2$
0
2
3
4
5
0
30
60
90
120
150
180
210
E/R
0
1
2
3
4
5

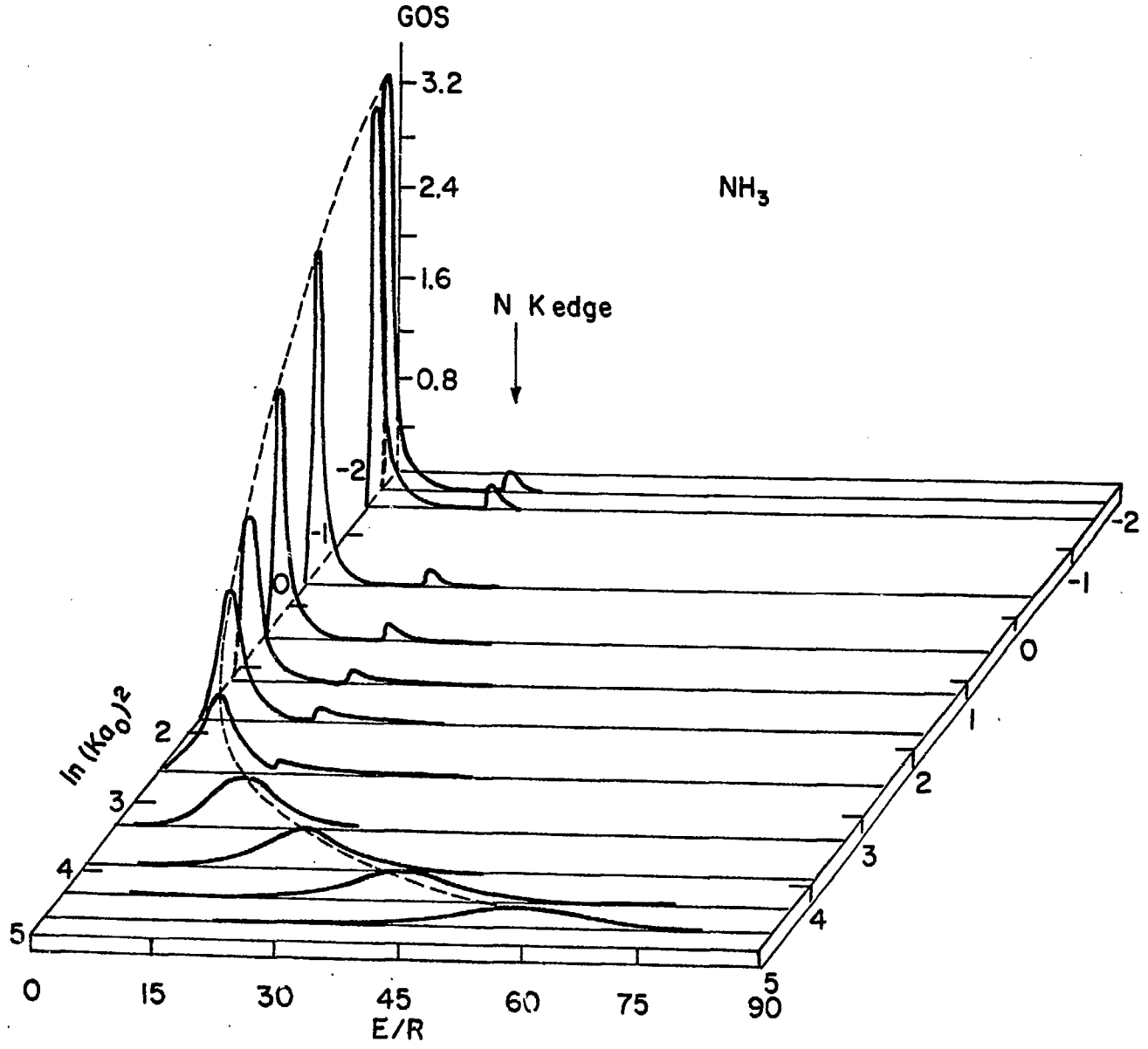
GOS
3.2
2.4
1.6
0.8
NH3
N K edge
-2
-1
0
1
2
3
4
5
ln(K0)2
0
15
30
45
60
75
90
E/R

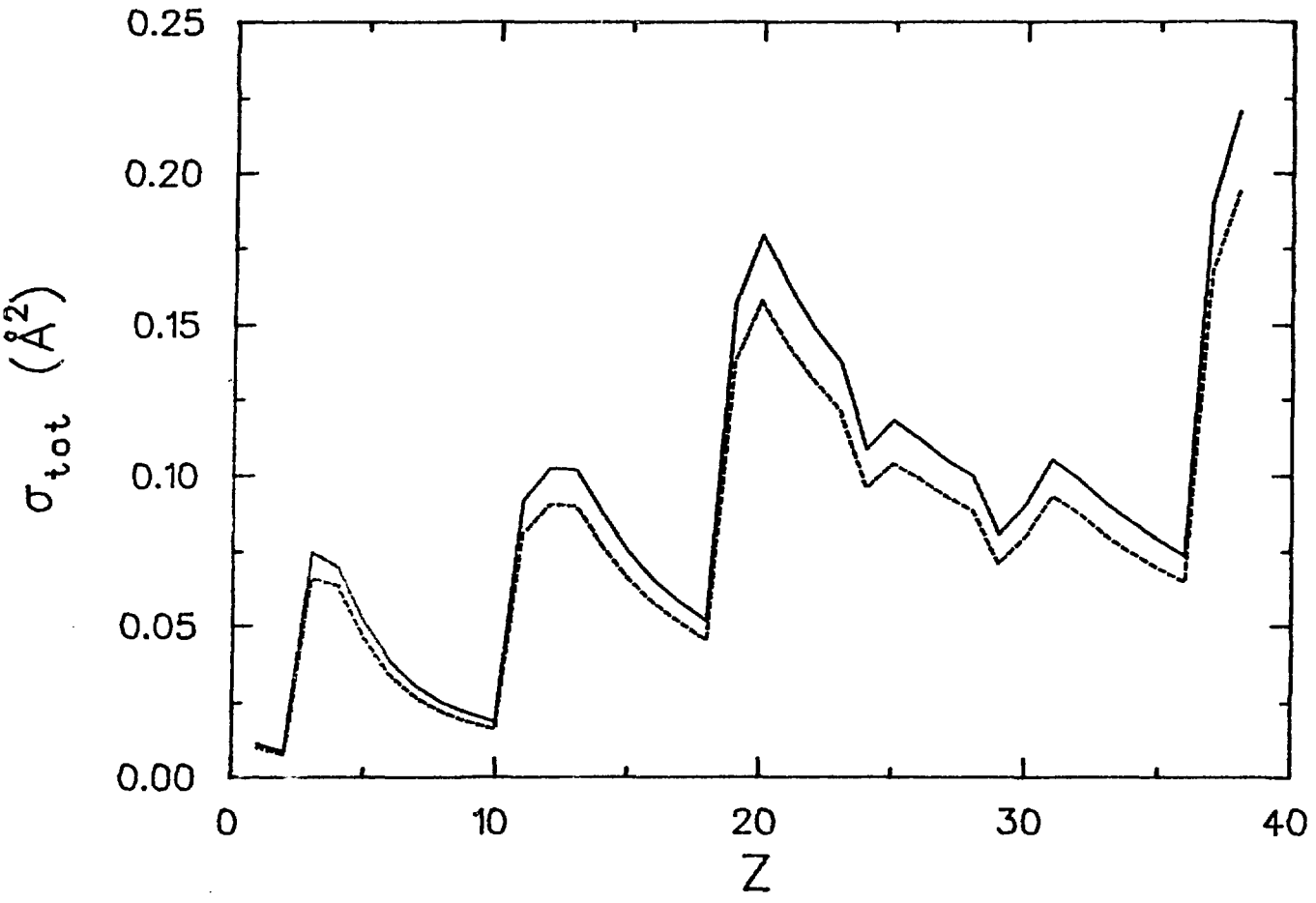
0.25
0.20
0.15
0.10
0.05
0.00
σtot (Å2)
0
10
20
30
40
Z

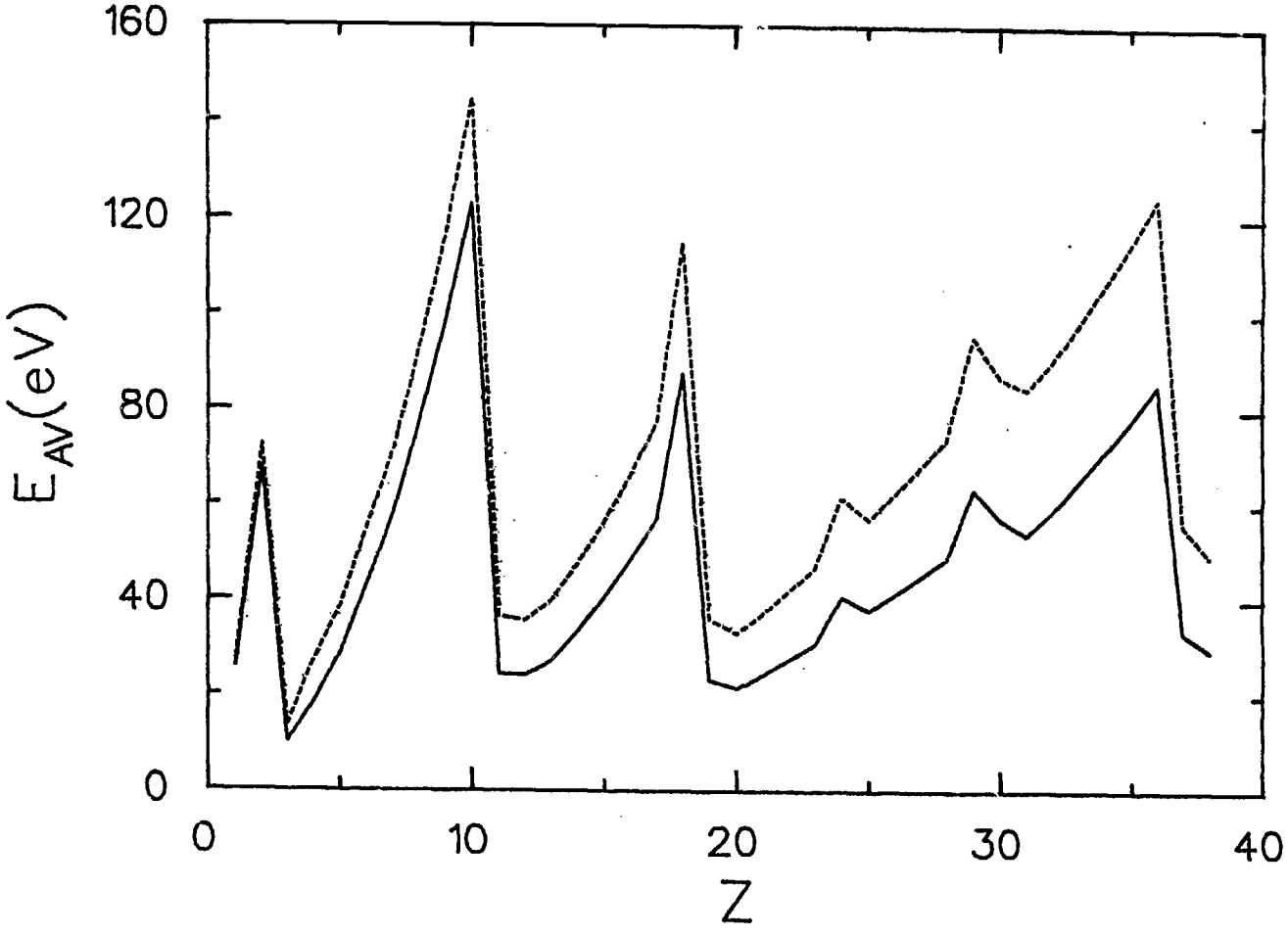
160
120
80
40
0
E_{AV}(eV)
0
10
20
30
40
Z

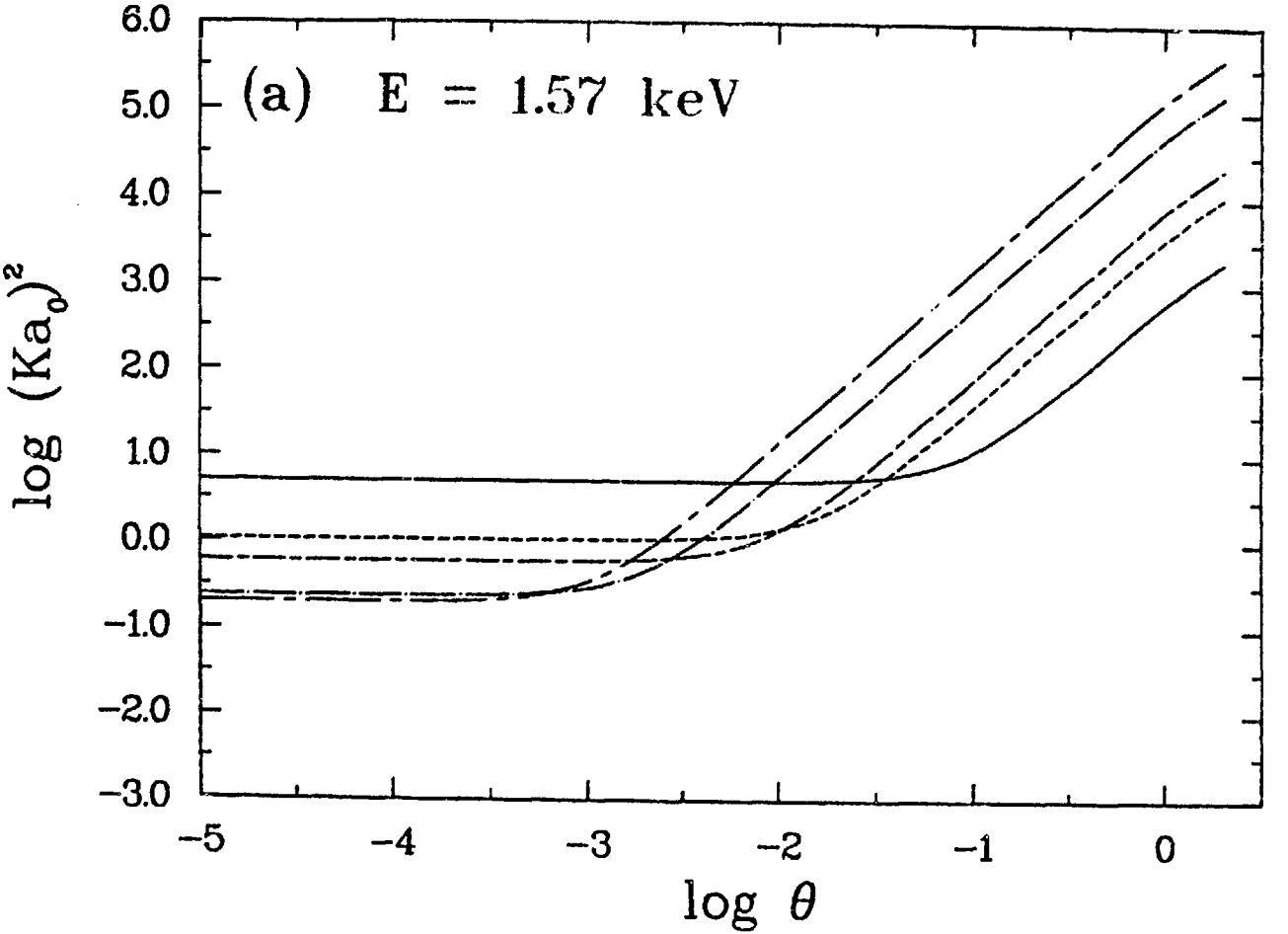
(a) E = 1.57 keV
6.0
5.0
4.0
3.0
2.0
1.0
0.0
−1.0
−2.0
−3.0
log $(Ka_0)^2$
−5
−4
−3
−2
−1
0
log θ

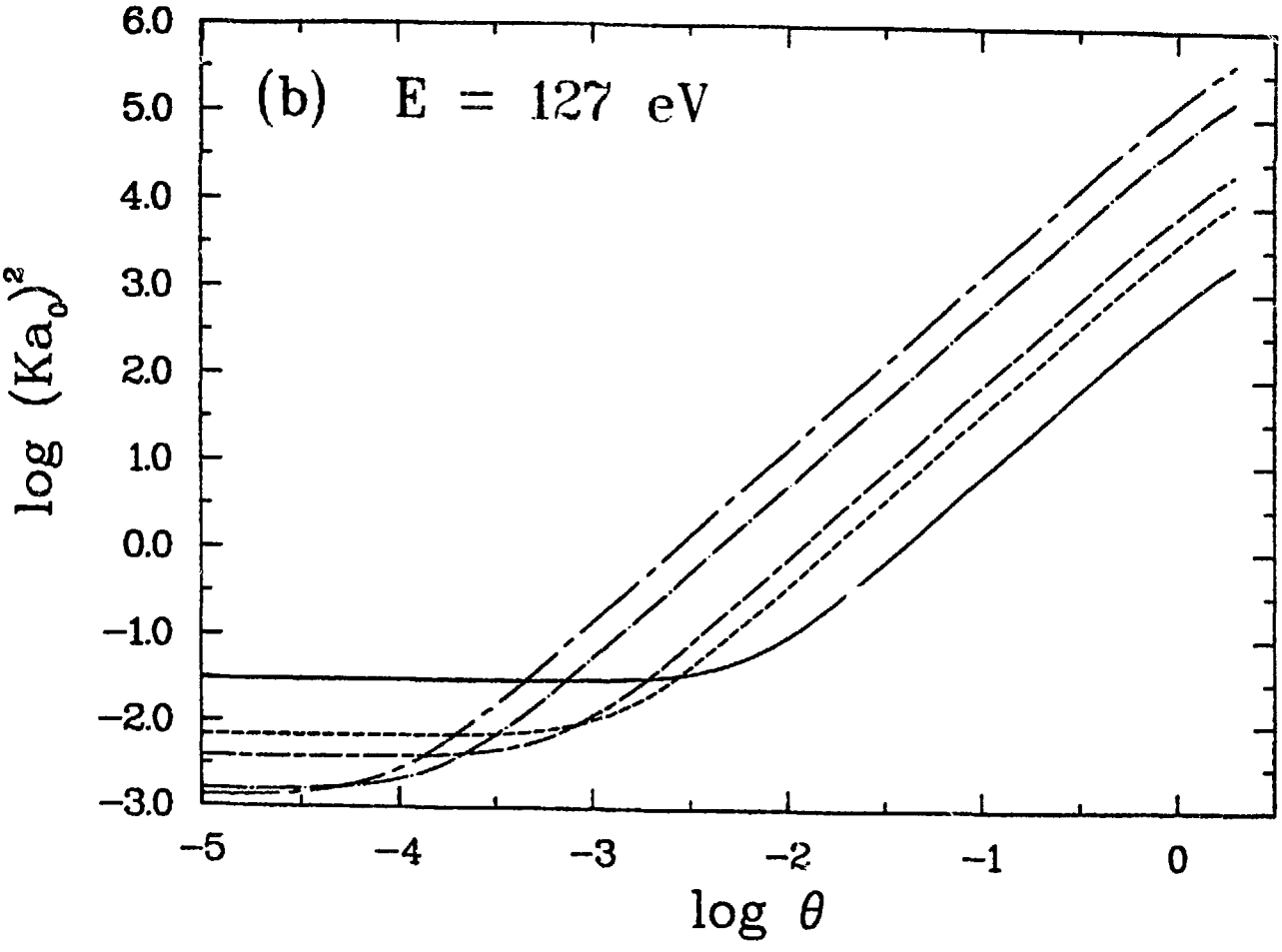
(b) E = 127 eV
6.0
5.0
4.0
3.0
2.0
1.0
0.0
−1.0
−2.0
−3.0
log $(Ka_0)^2$
−5
−4
−3
−2
−1
0
log θ

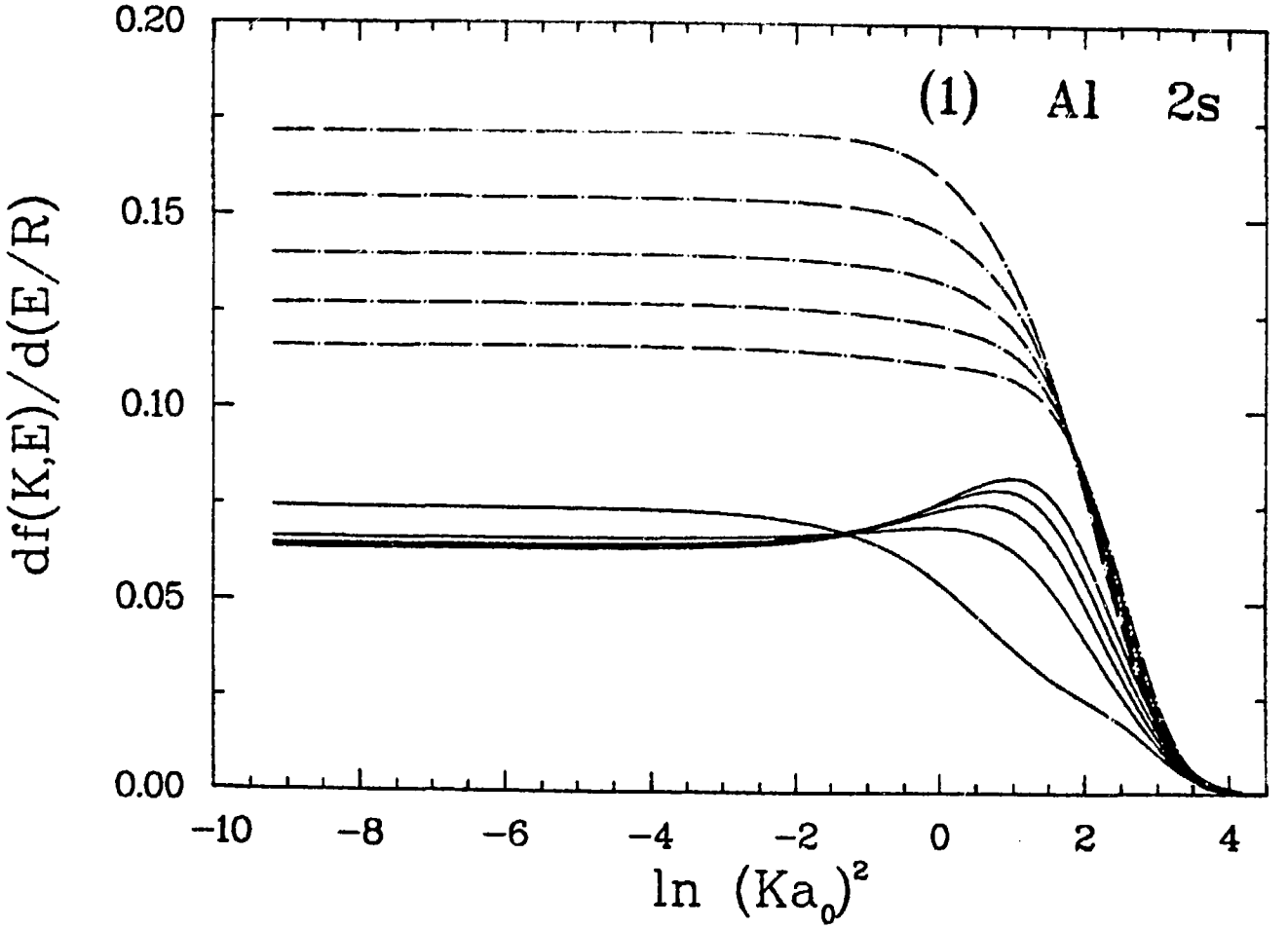
(1) Al 2s
0.20
0.15
0.10
0.05
0.00
df(K,E)/d(E/R)
−10
−8
−6
−4
−2
0
2
4
ln (Ka0)2

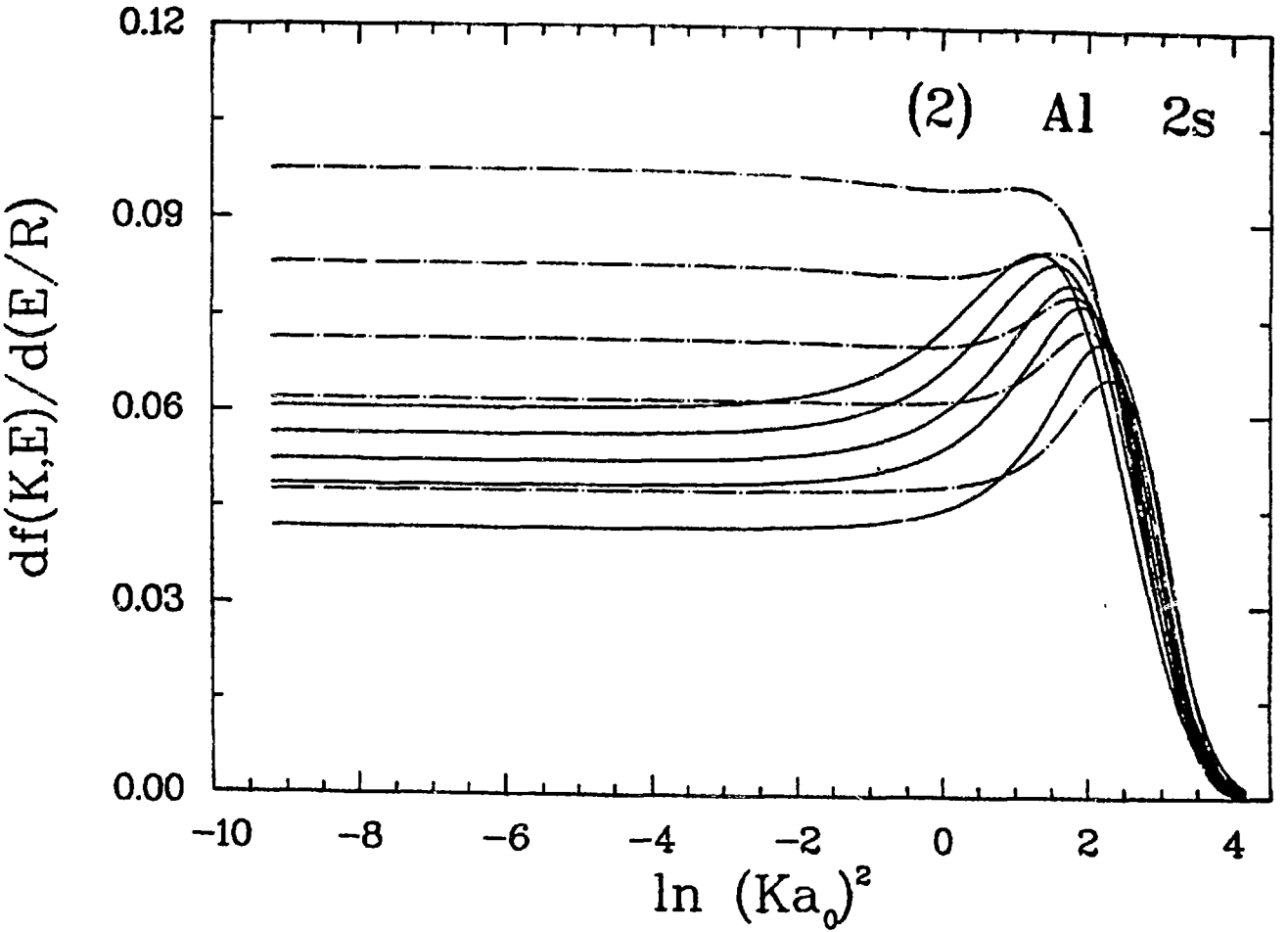
(2) Al 2s
0.12
0.09
0.06
0.03
0.00
df(K,E)/d(E/R)
−10
−8
−6
−4
−2
0
2
4
ln (Ka0)²

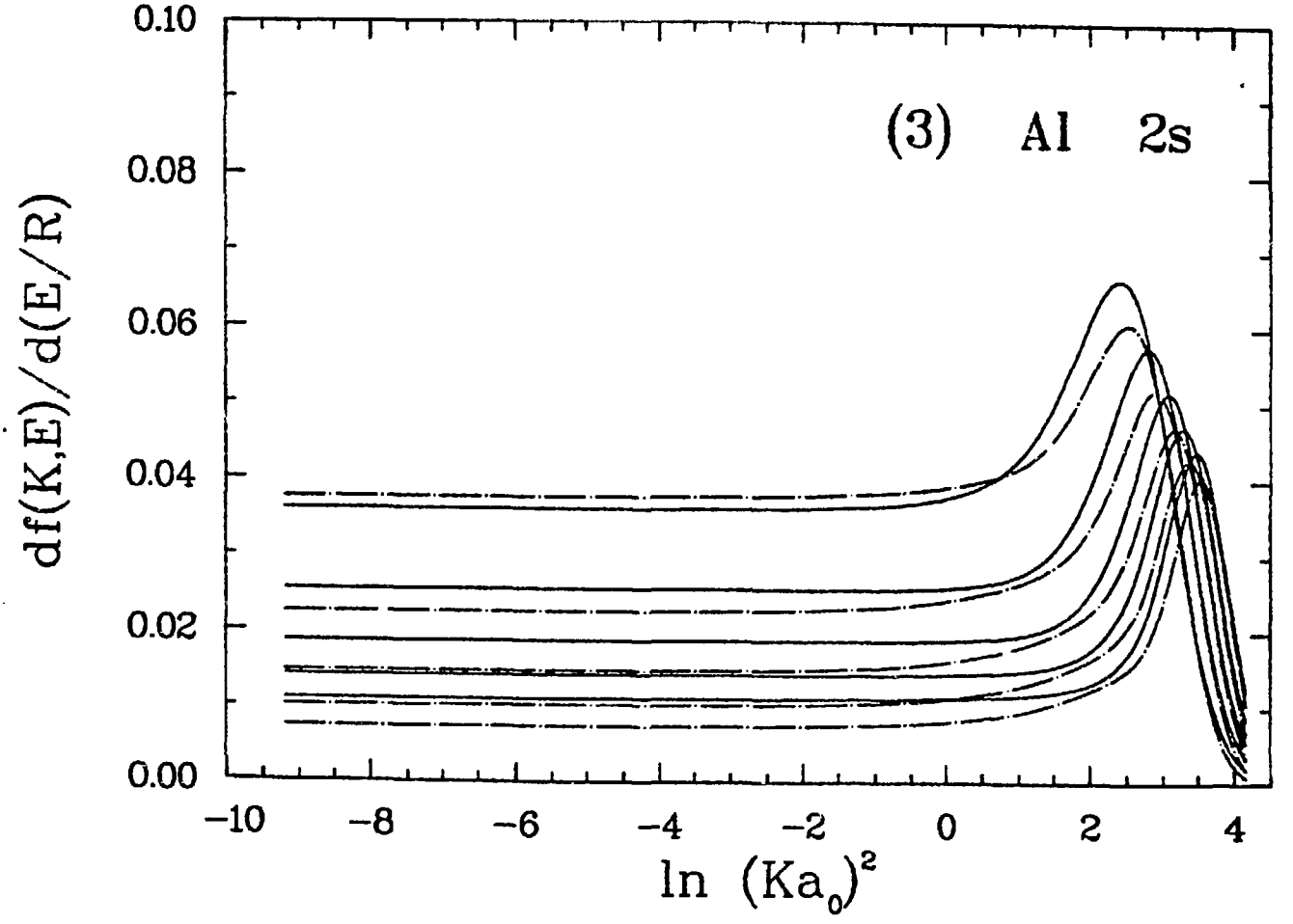
(3) Al 2s
df(K,E)/d(E/R)
0.10
0.08
0.06
0.04
0.02
0.00
−10
−8
−6
−4
−2
0
2
4
ln (Ka0)2

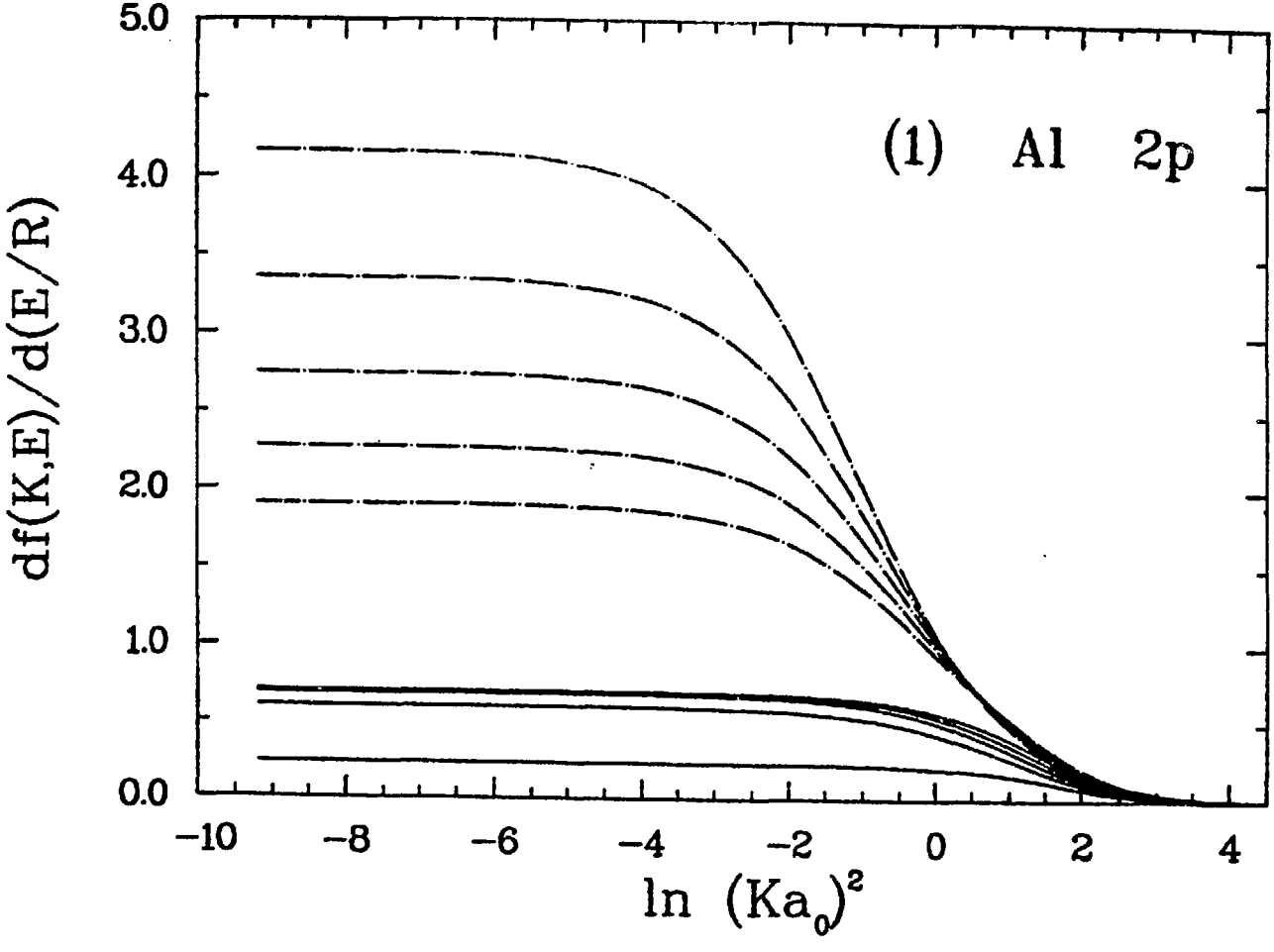
(1) Al 2p
df(K,E)/d(E/R)
5.0
4.0
3.0
2.0
1.0
0.0
−10
−8
−6
−4
−2
0
2
4
ln (Ka0)2

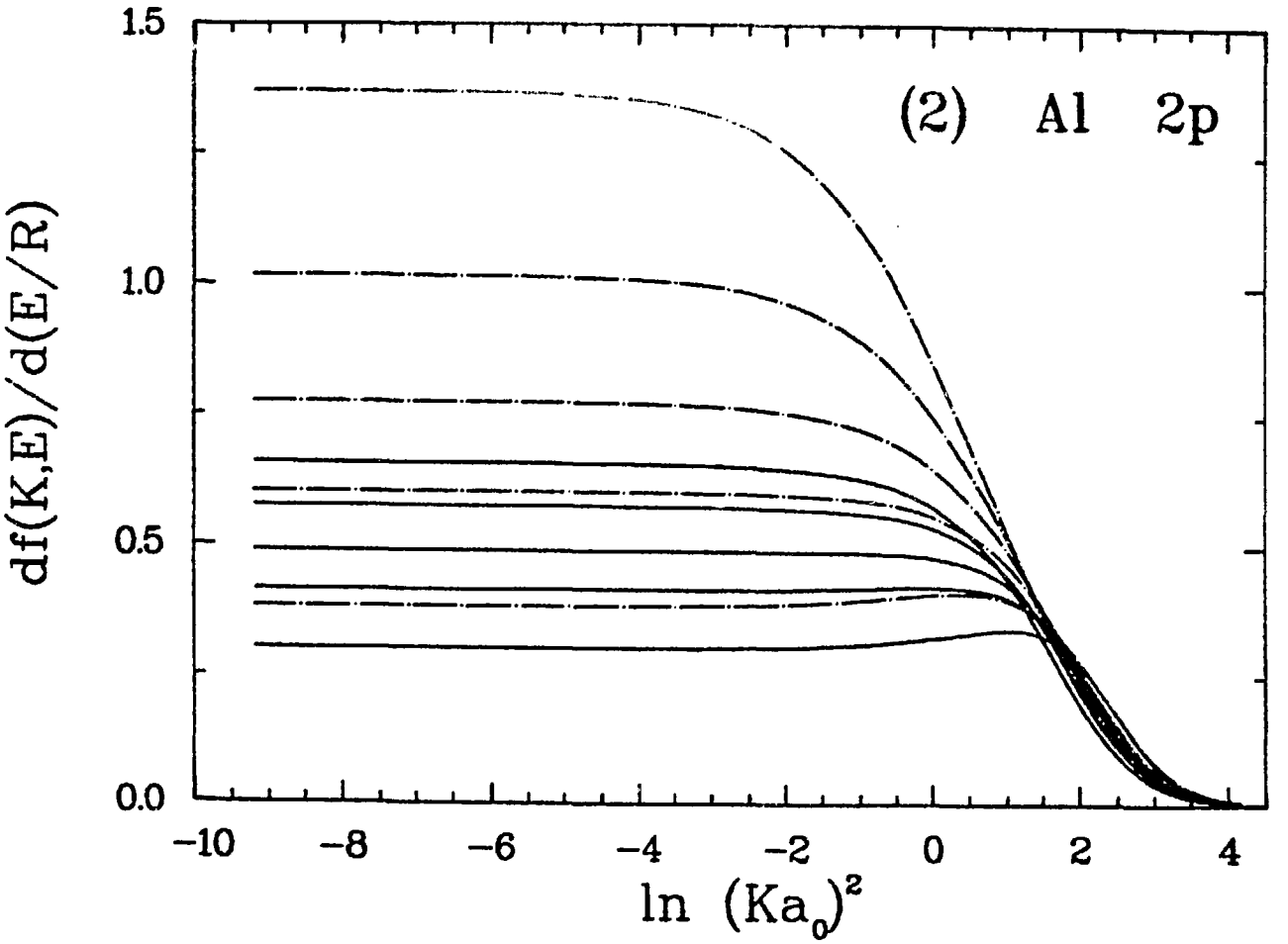
(2) Al 2p
df(K,E)/d(E/R)
1.5
1.0
0.5
0.0
−10
−8
−6
−4
−2
0
2
4
ln (Ka0)2

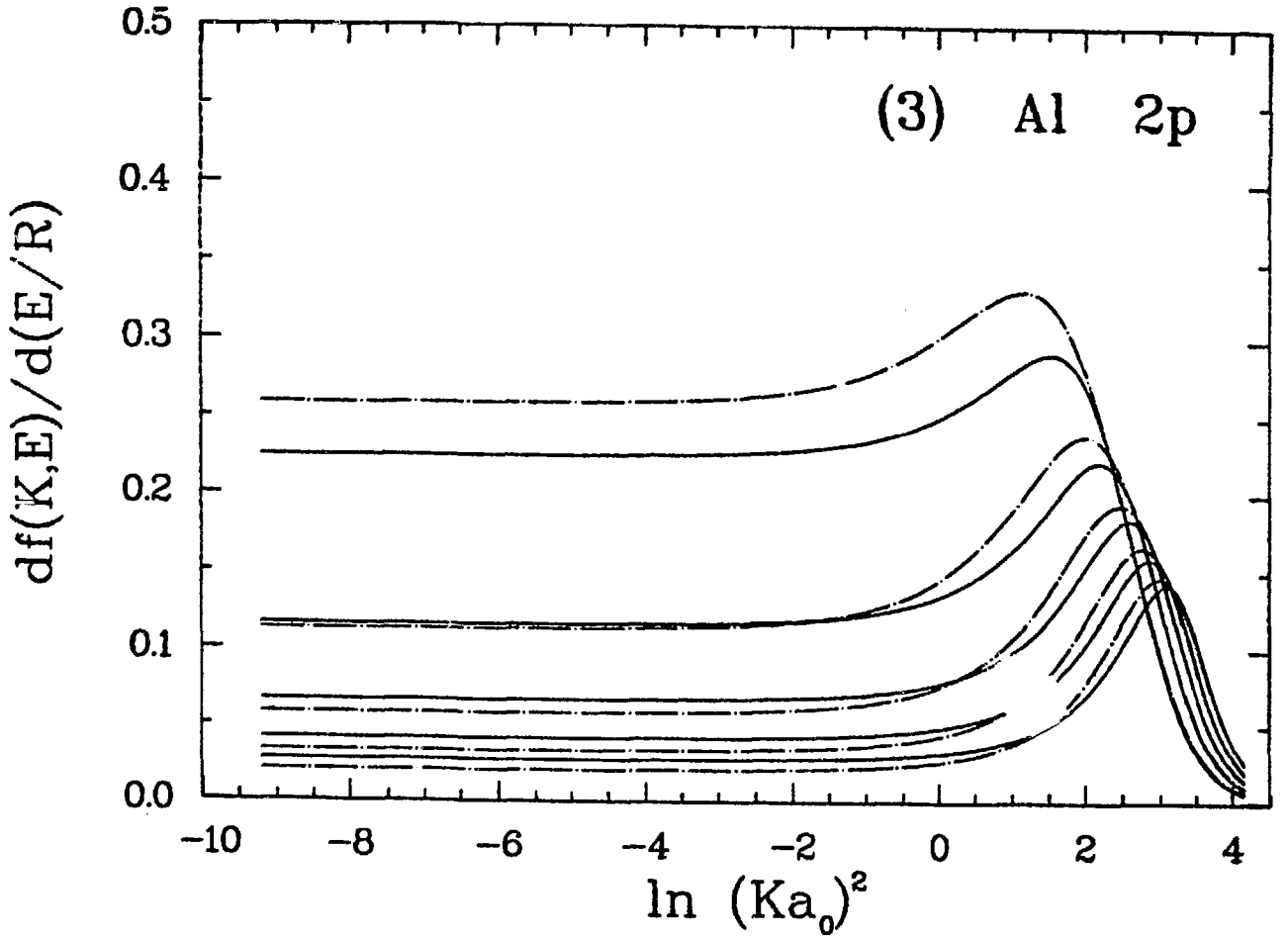
(3) Al 2p
df(K,E)/d(E/R)
0.5
0.4
0.3
0.2
0.1
0.0
−10
−8
−6
−4
−2
0
2
4
ln (Ka0)2

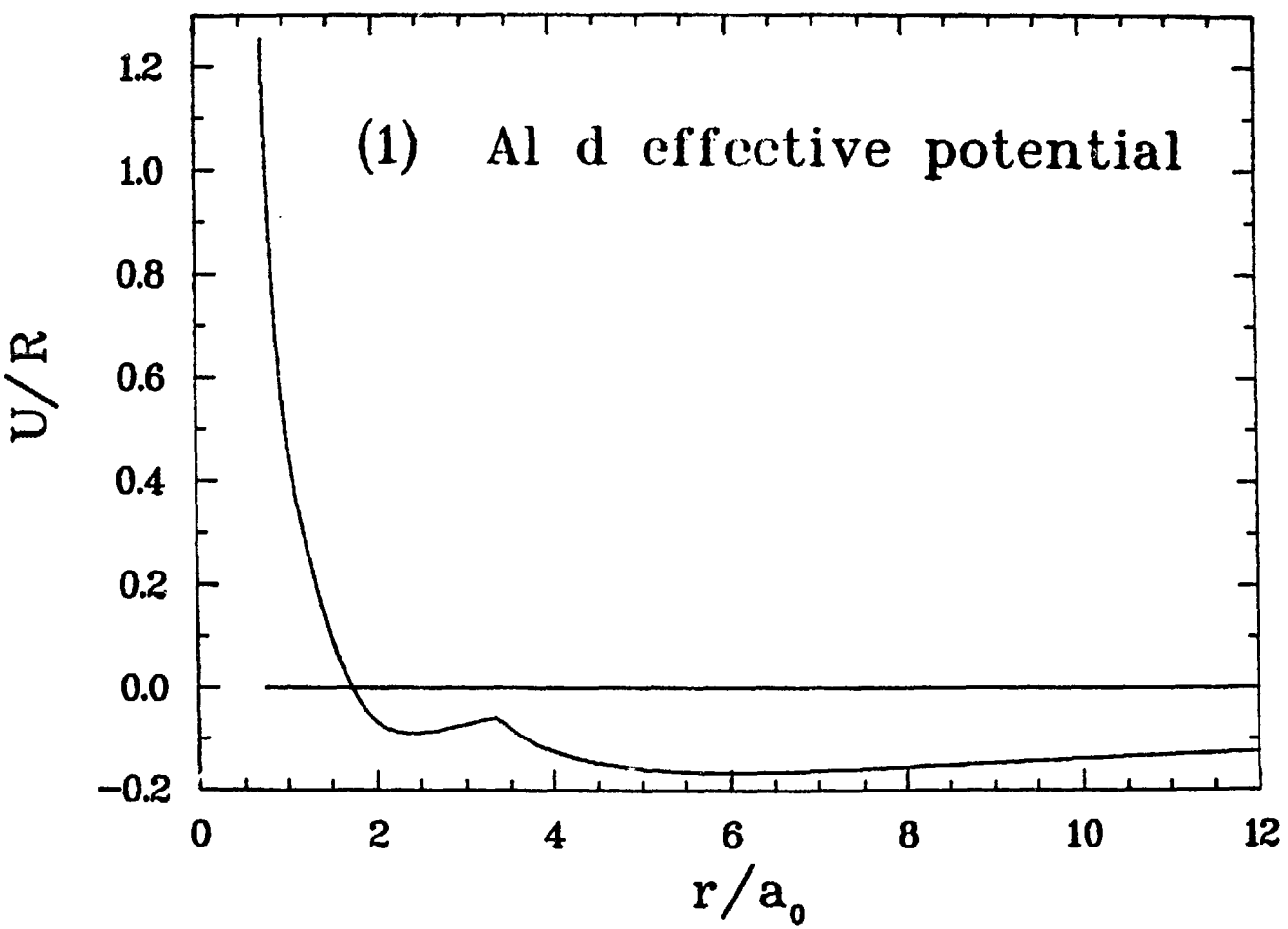
(1) Al d effective potential
U/R
1.2
1.0
0.8
0.6
0.4
0.2
0.0
-0.2
0
2
4
6
8
10
12
r/a0

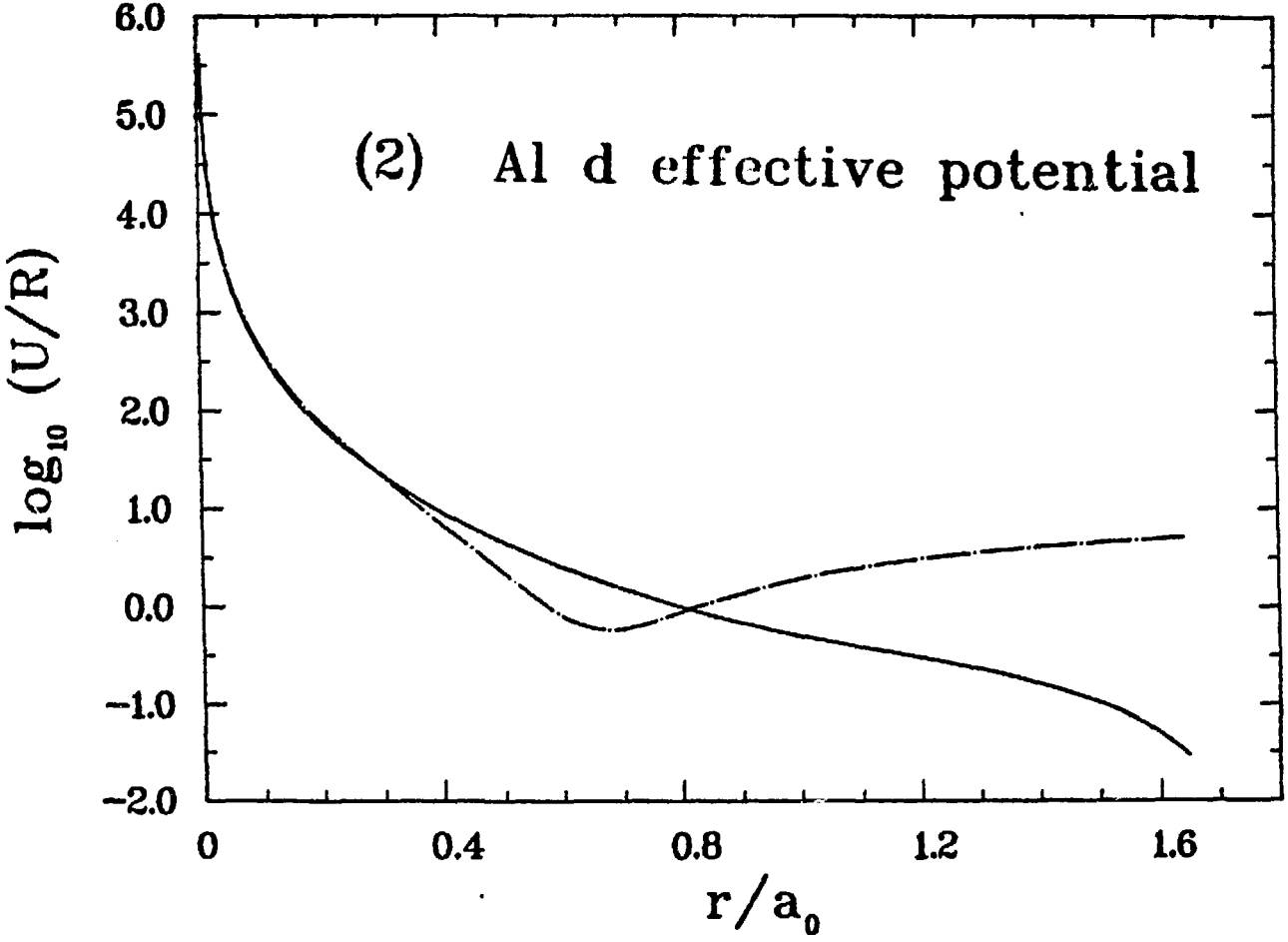
(2) Al d effective potential
6.0
5.0
4.0
3.0
2.0
1.0
0.0
−1.0
−2.0
log10 (U/R)
0
0.4
0.8
1.2
1.6
r/a0

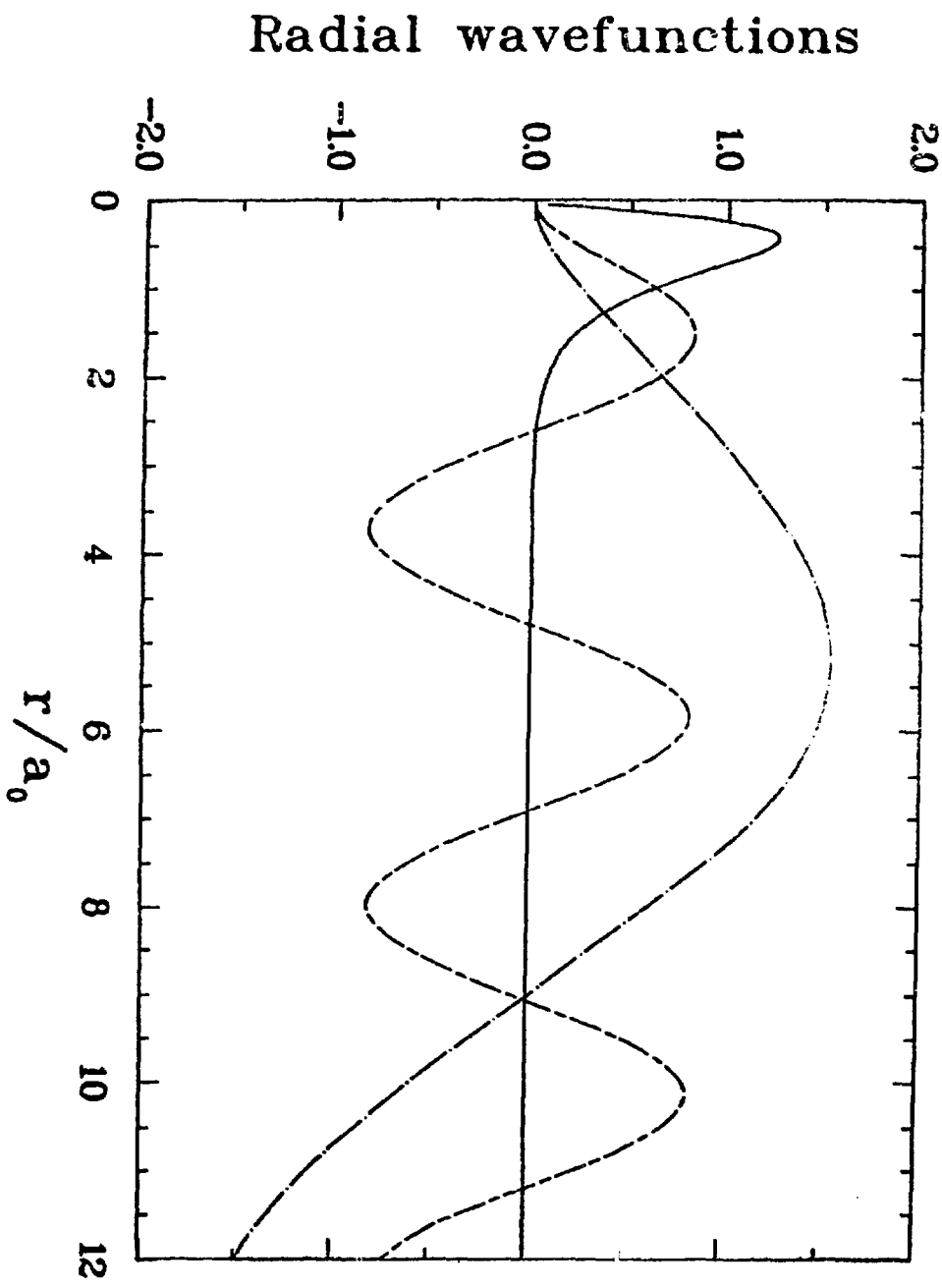
Radial wavefunctions
-2.0
-1.0
0.0
1.0
2.0
0
2
4
6
8
10
12
r/a0

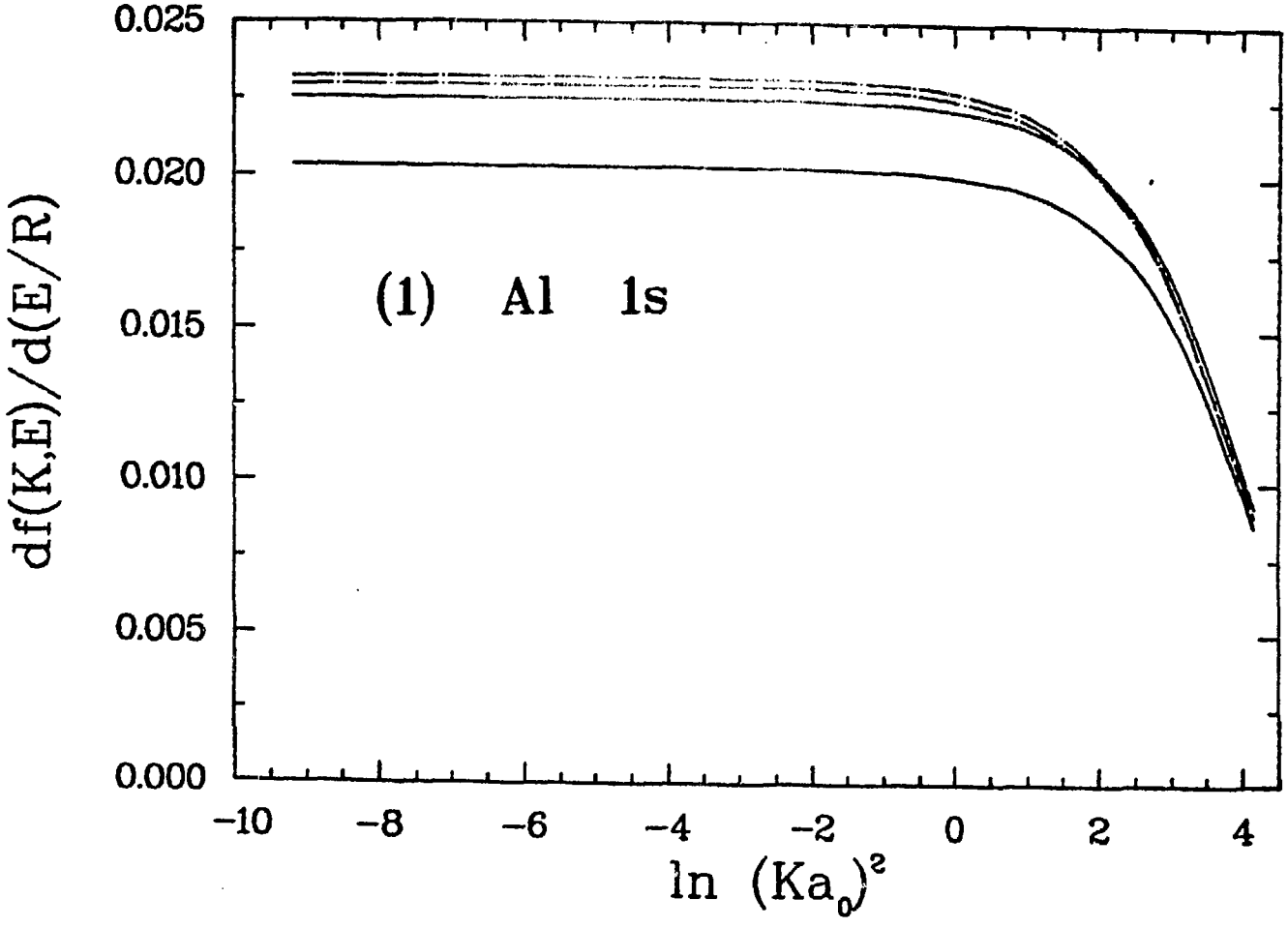
0.025
0.020
0.015
0.010
0.005
0.000
df(K,E)/d(E/R)
(1) Al 1s
−10
−8
−6
−4
−2
0
2
4
ln (Ka0)2

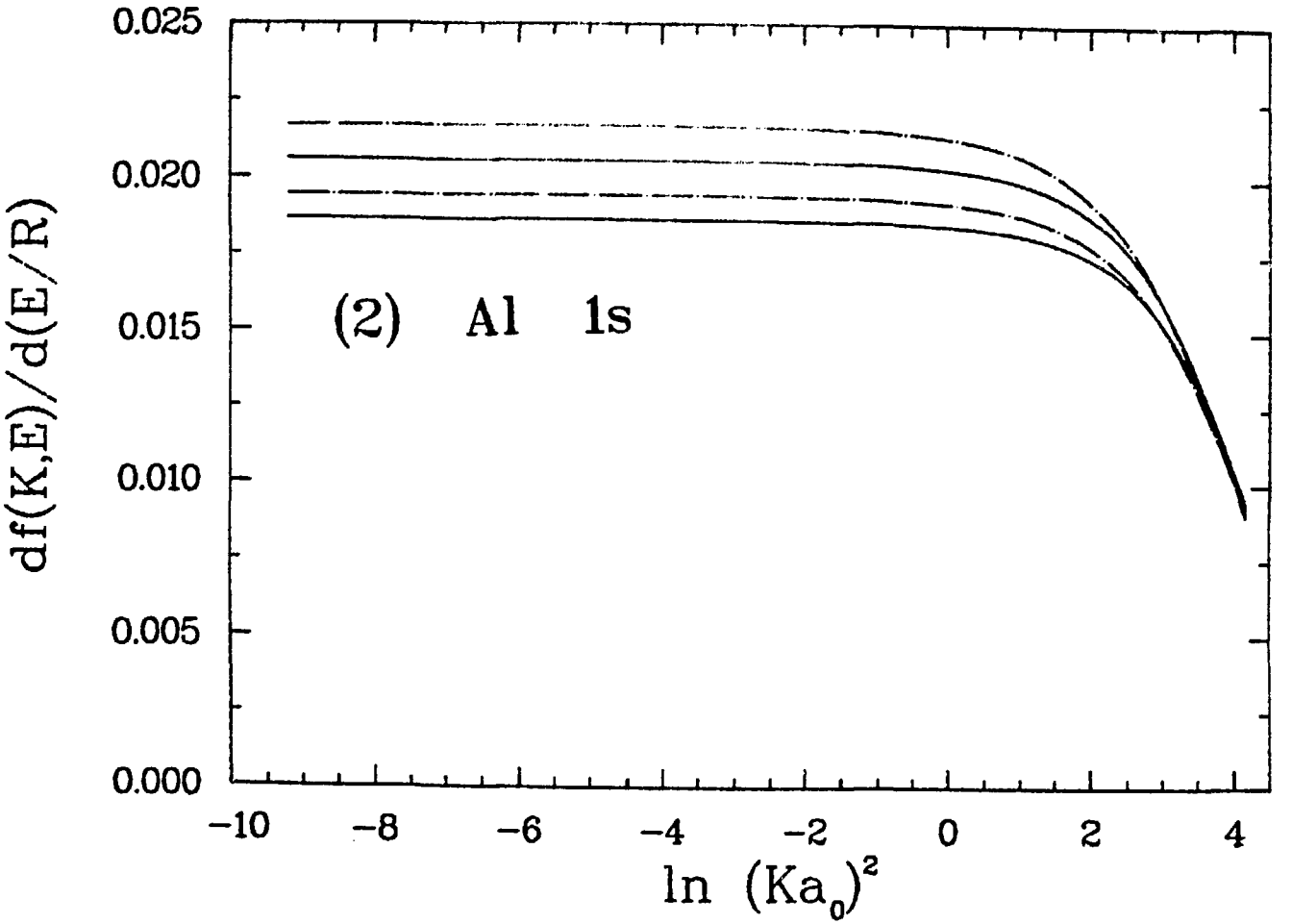
0.025
0.020
0.015
0.010
0.005
0.000
df(K,E)/d(E/R)
(2) Al 1s
−10
−8
−6
−4
−2
0
2
4
ln (Ka0)2

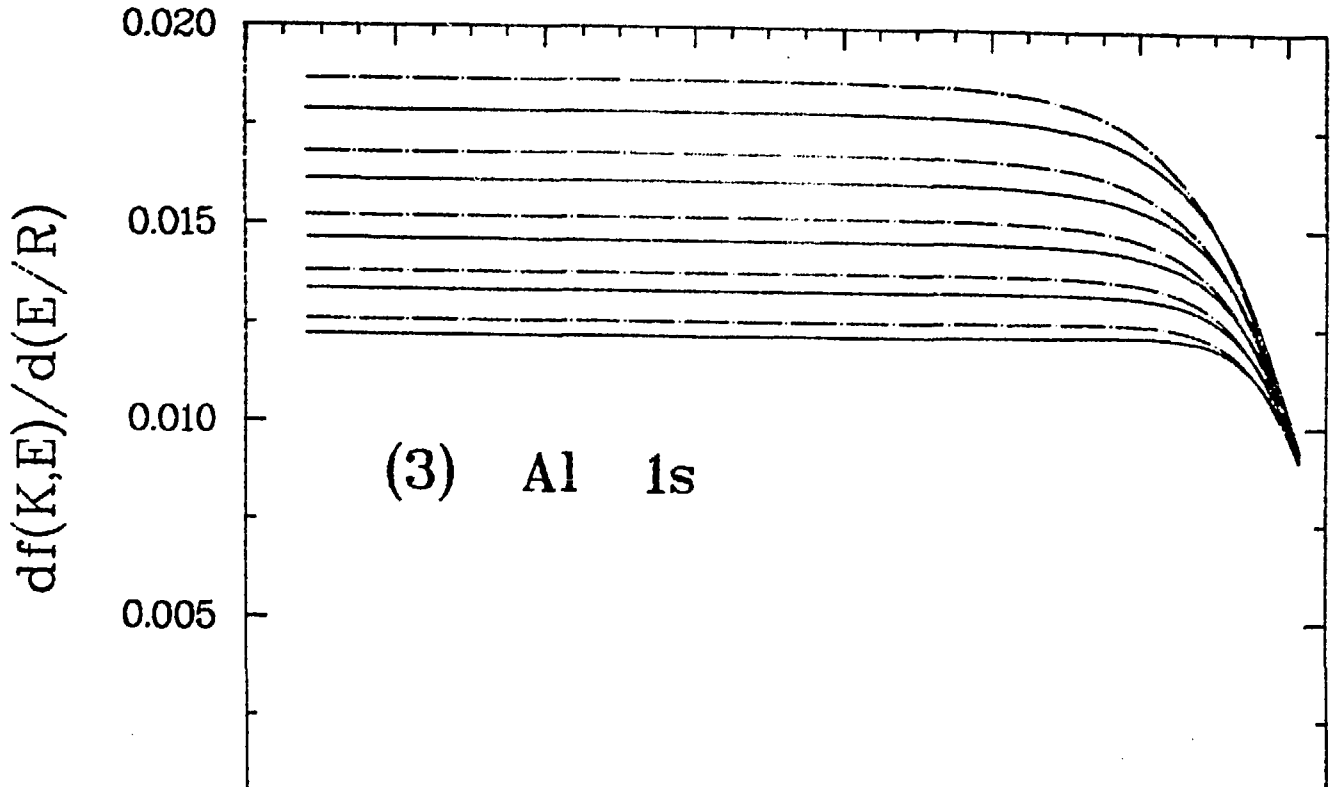
0.020
0.015
0.010
0.005
0.000
df(K,E)/d(E/R)
(3) Al 1s
−10
−8
−6
−4
−2
0
2
4
ln (Ka0)2

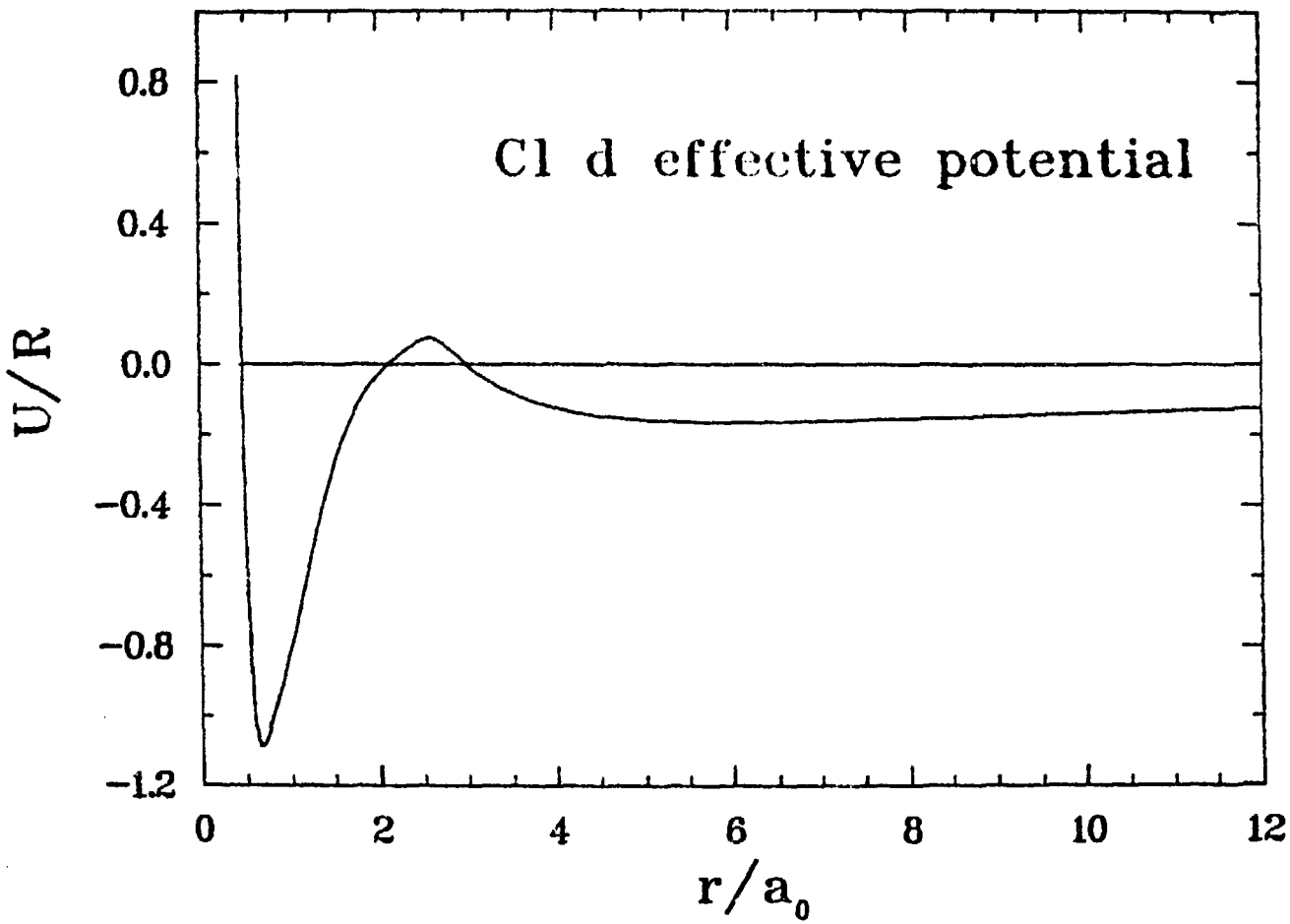
Cl d effective potential
U/R
0.8
0.4
0.0
−0.4
−0.8
−1.2
0
2
4
6
8
10
12
r/a0

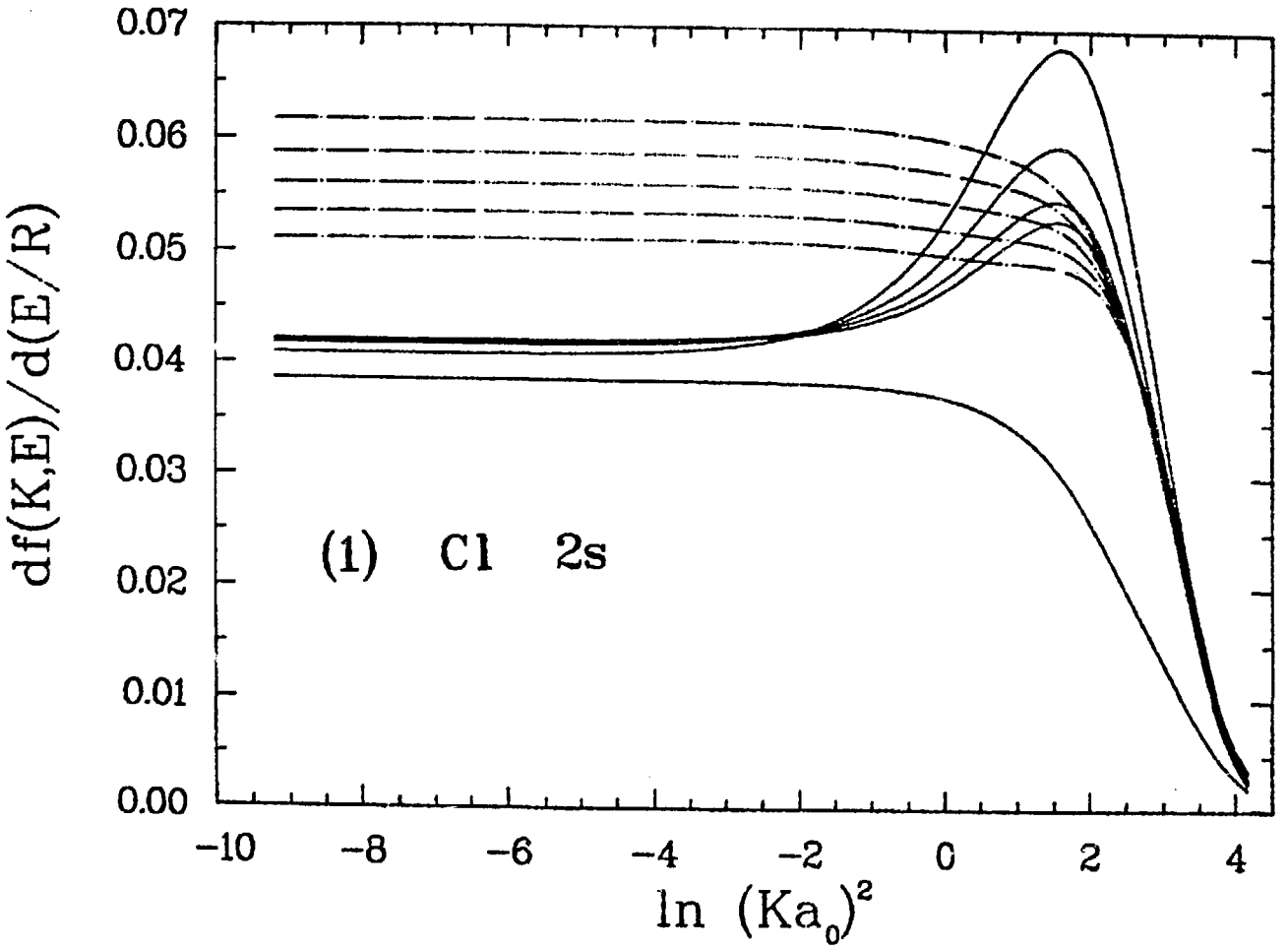
0.07
0.06
0.05
0.04
0.03
0.02
0.01
0.00
df(K,E)/d(E/R)
(1) Cl 2s
−10
−8
−6
−4
−2
0
2
4
ln (Ka0)2

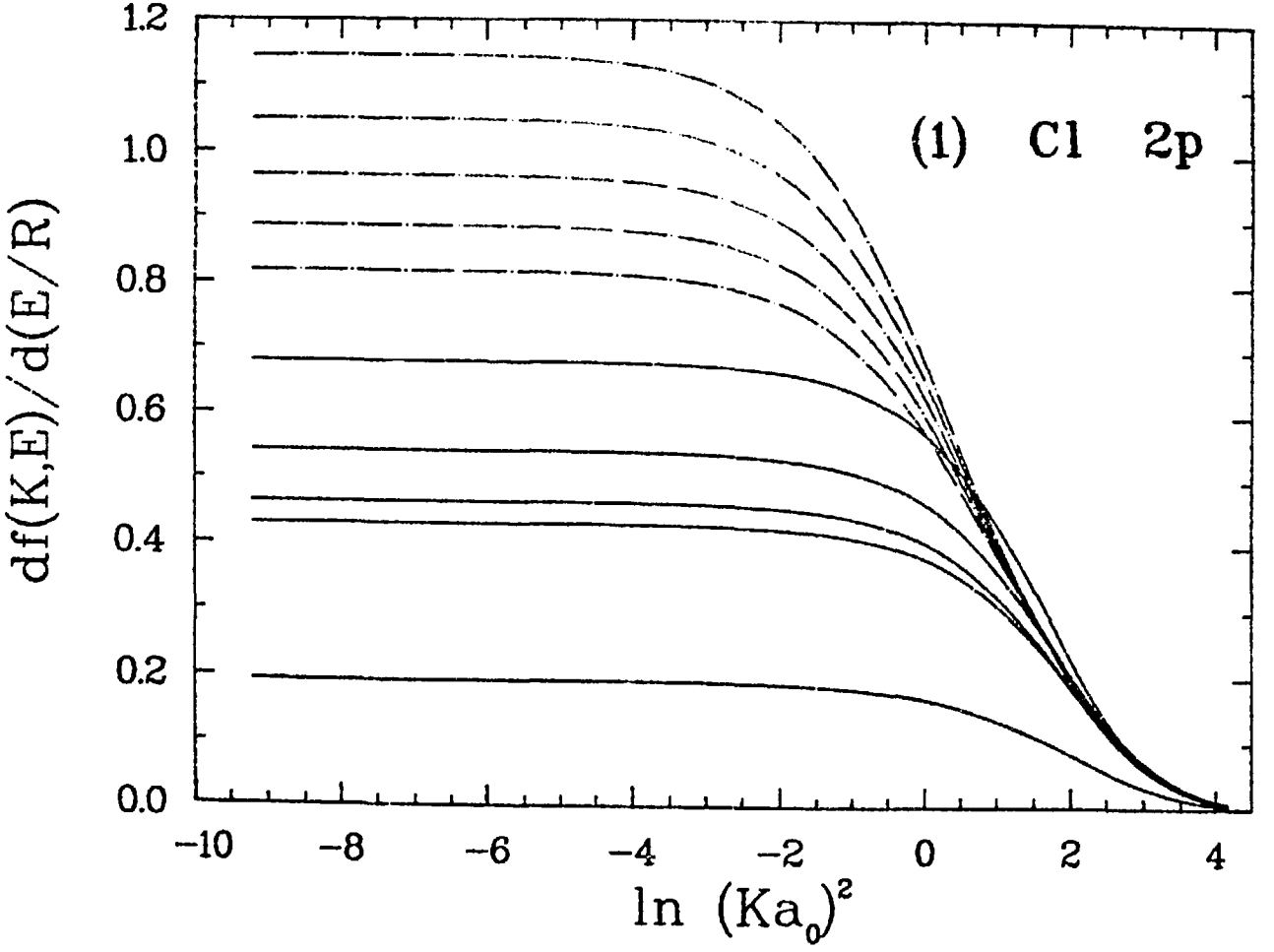
(1) Cl 2p
df(K,E)/d(E/R)
ln (Ka0)2
1.2
1.0
0.8
0.6
0.4
0.2
0.0
−10
−8
−6
−4
−2
0
2
4

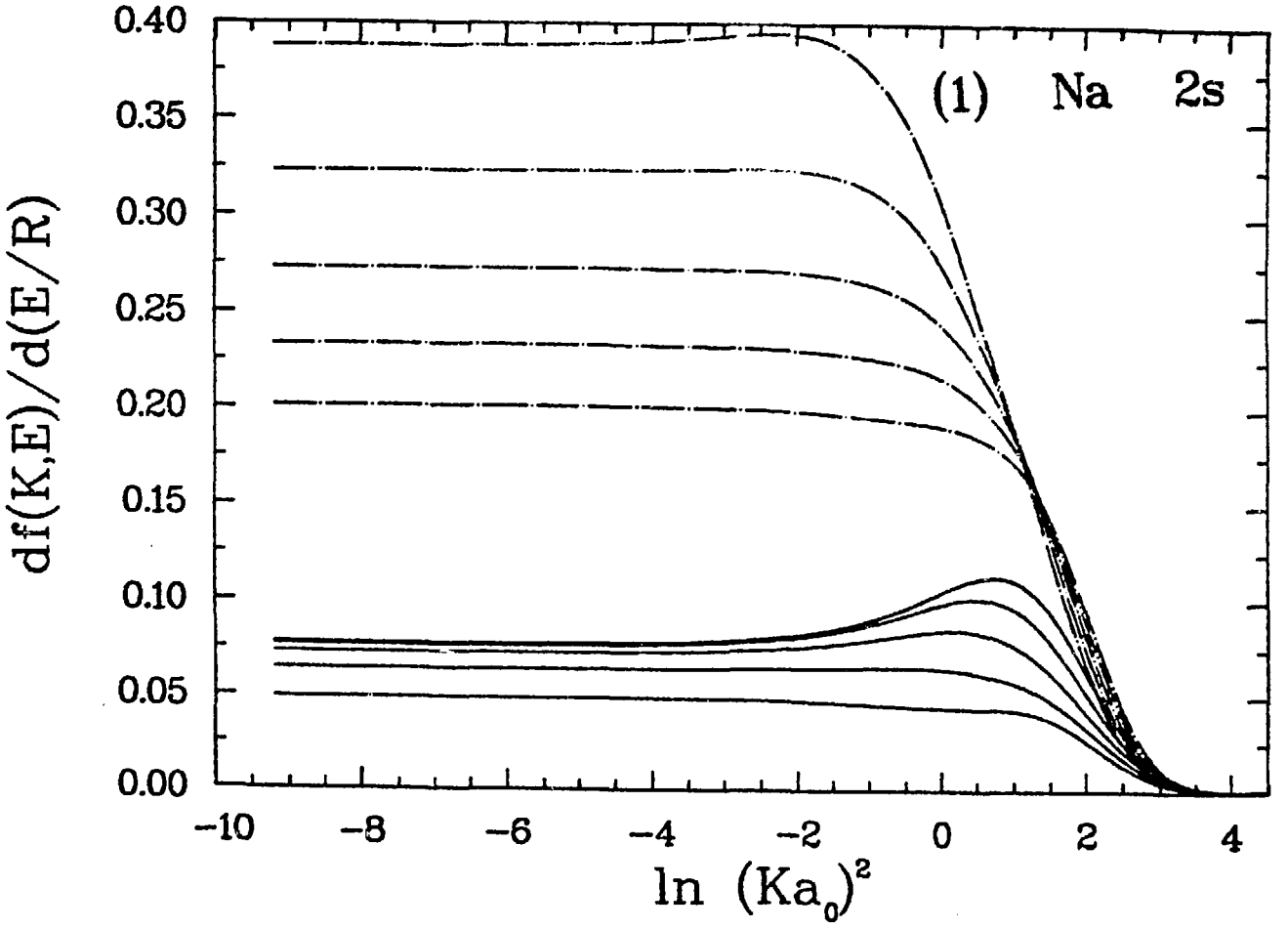
(1) Na 2s
df(K,E)/d(E/R)
0.40
0.35
0.30
0.25
0.20
0.15
0.10
0.05
0.00
−10
−8
−6
−4
−2
0
2
4
ln (Ka0)2

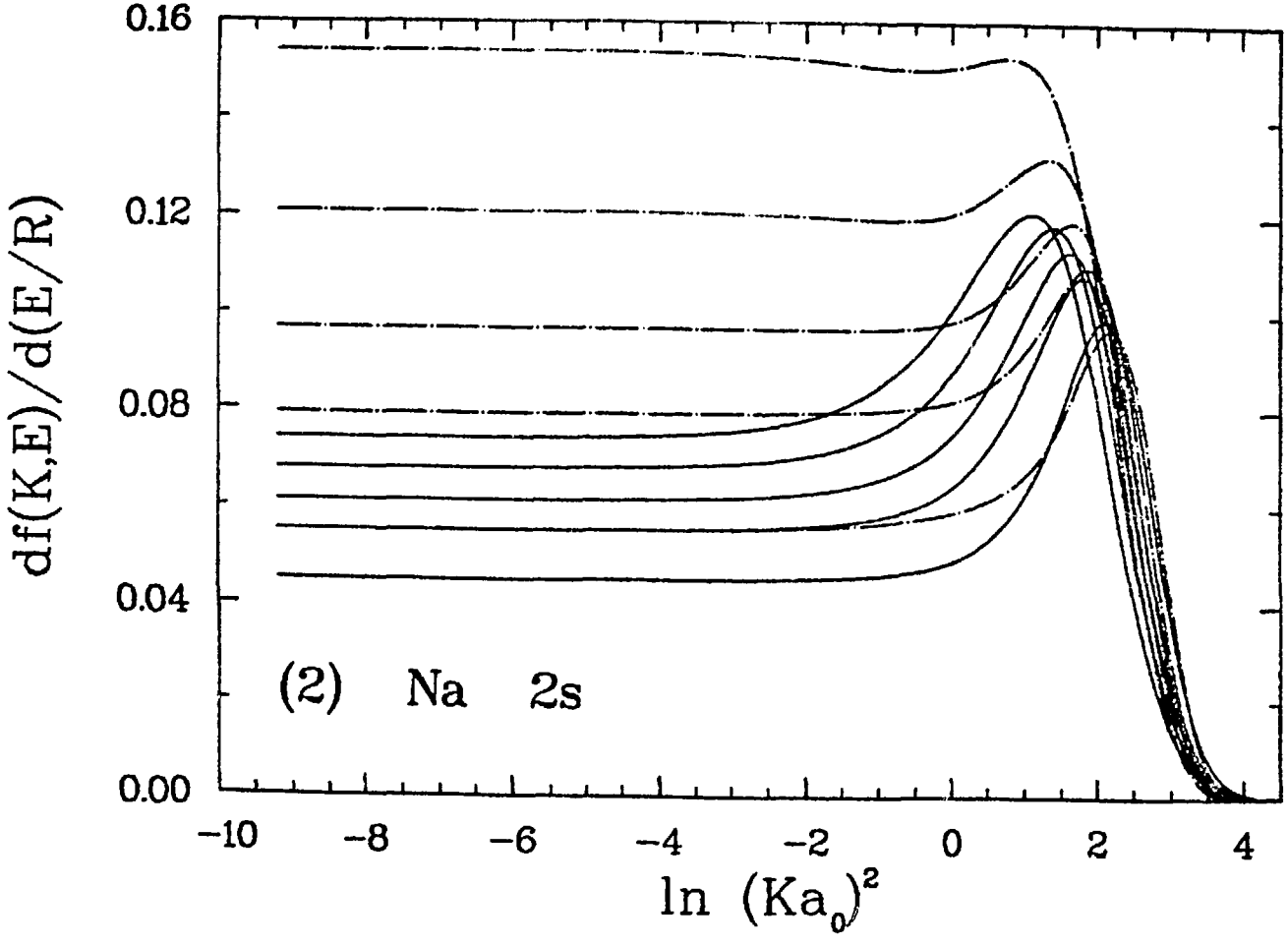
0.16
0.12
0.08
0.04
0.00
df(K,E)/d(E/R)
(2) Na 2s
−10
−8
−6
−4
−2
0
2
4
ln (Ka0)2

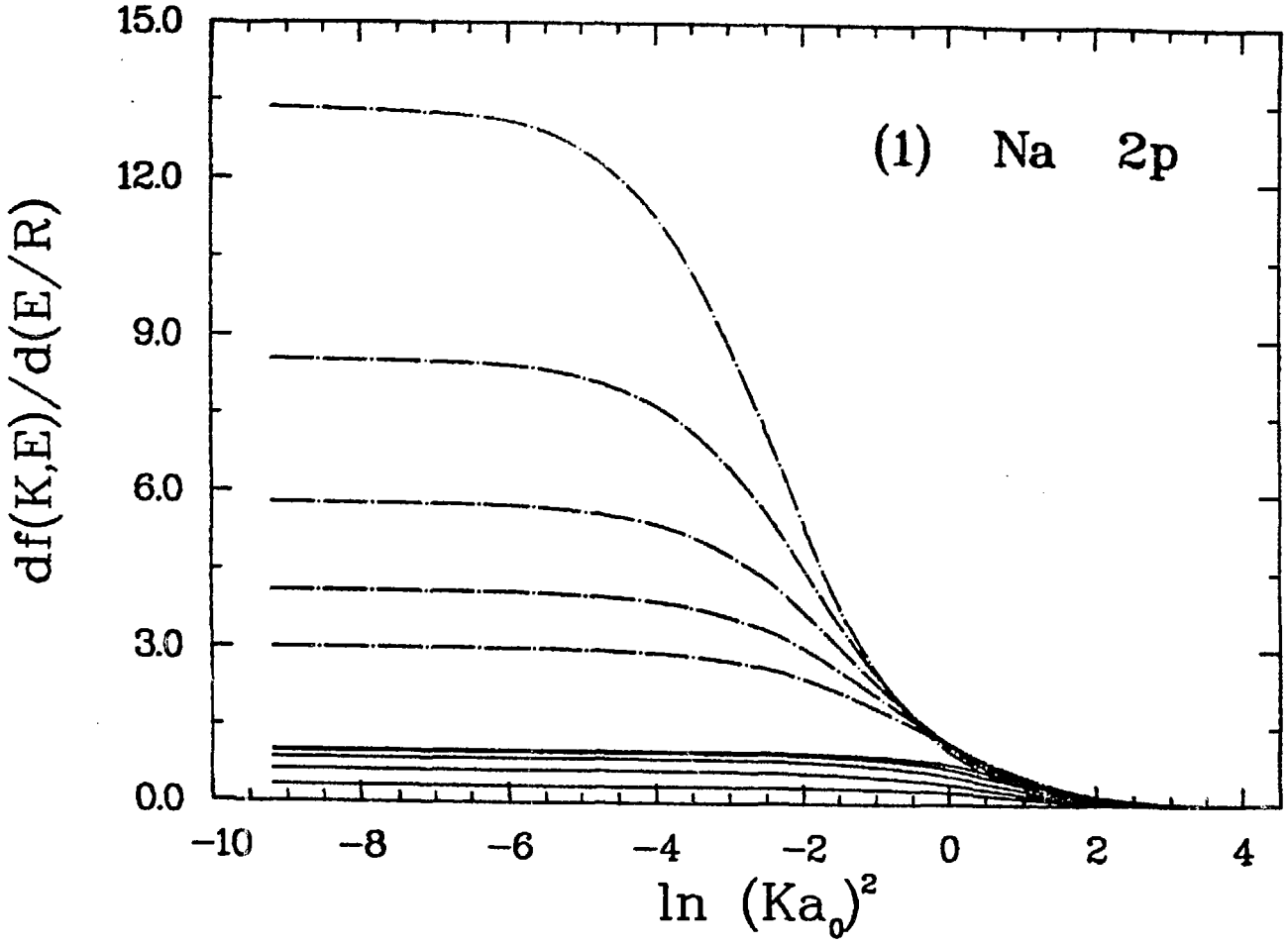
15.0
12.0
9.0
6.0
3.0
0.0
df(K,E)/d(E/R)
(1) Na 2p
−10
−8
−6
−4
−2
0
2
4
ln (Ka0)2

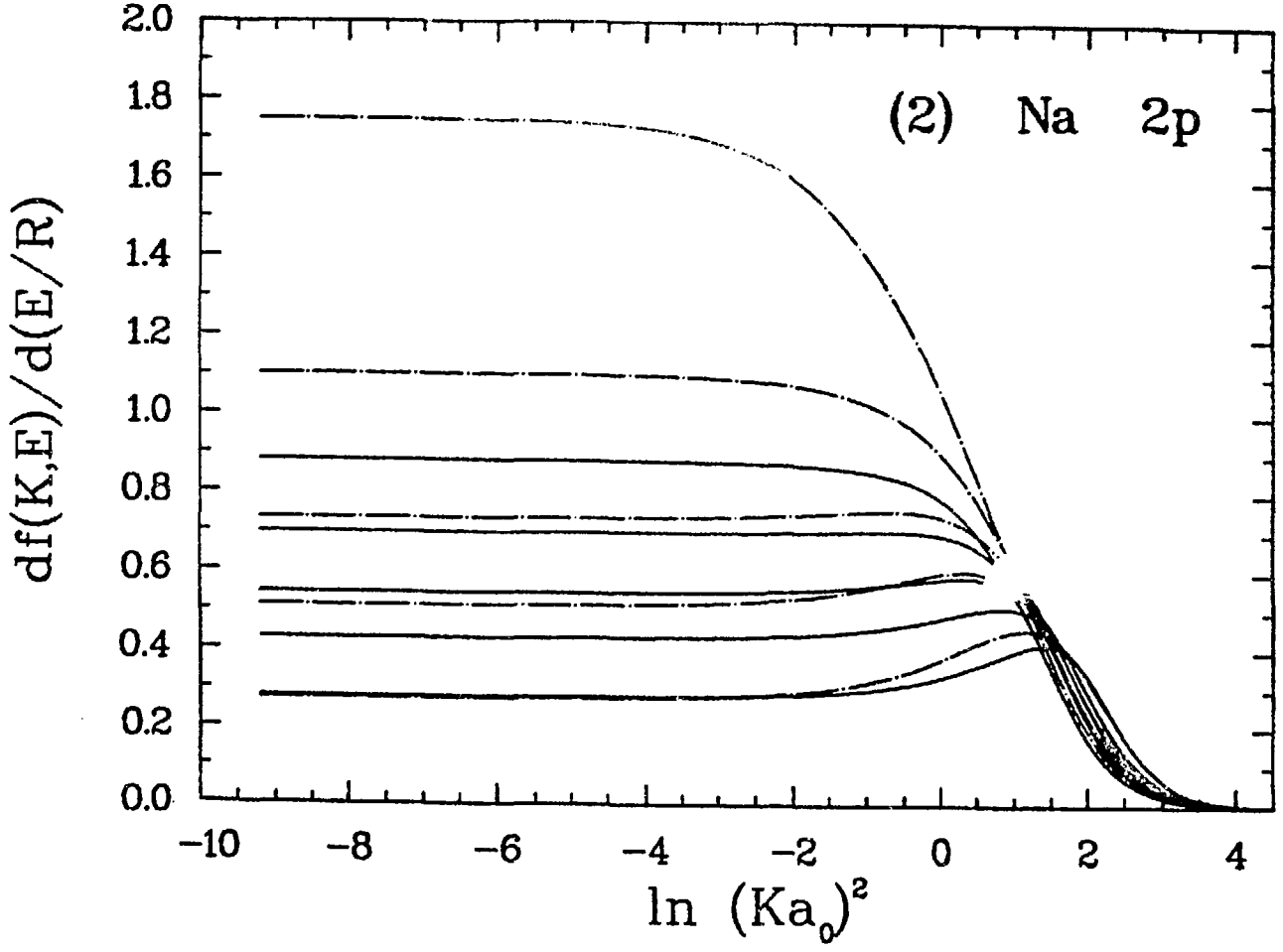
(2) Na 2p
df(K,E)/d(E/R)
2.0
1.8
1.6
1.4
1.2
1.0
0.8
0.6
0.4
0.2
0.0
−10
−8
−6
−4
−2
0
2
4
ln (Ka0)2

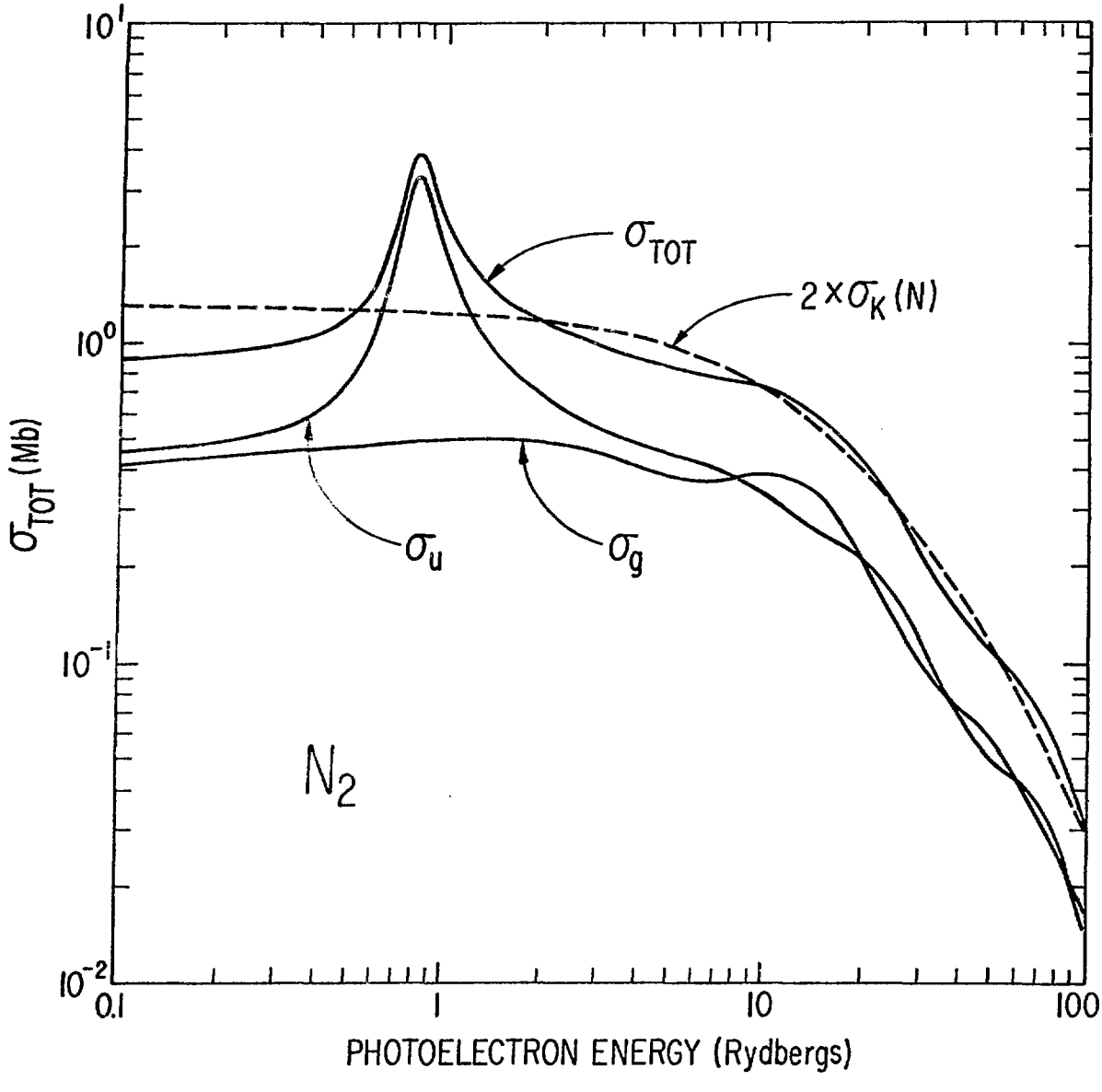
10^1
10^0
10^{-1}
10^{-2}
σ_{TOT} (Mb)
σ_{TOT}
$2\times\sigma_K(N)$
σ_u
σ_g
N_2
0.1
1
10
100
PHOTOELECTRON ENERGY (Rydbergs)

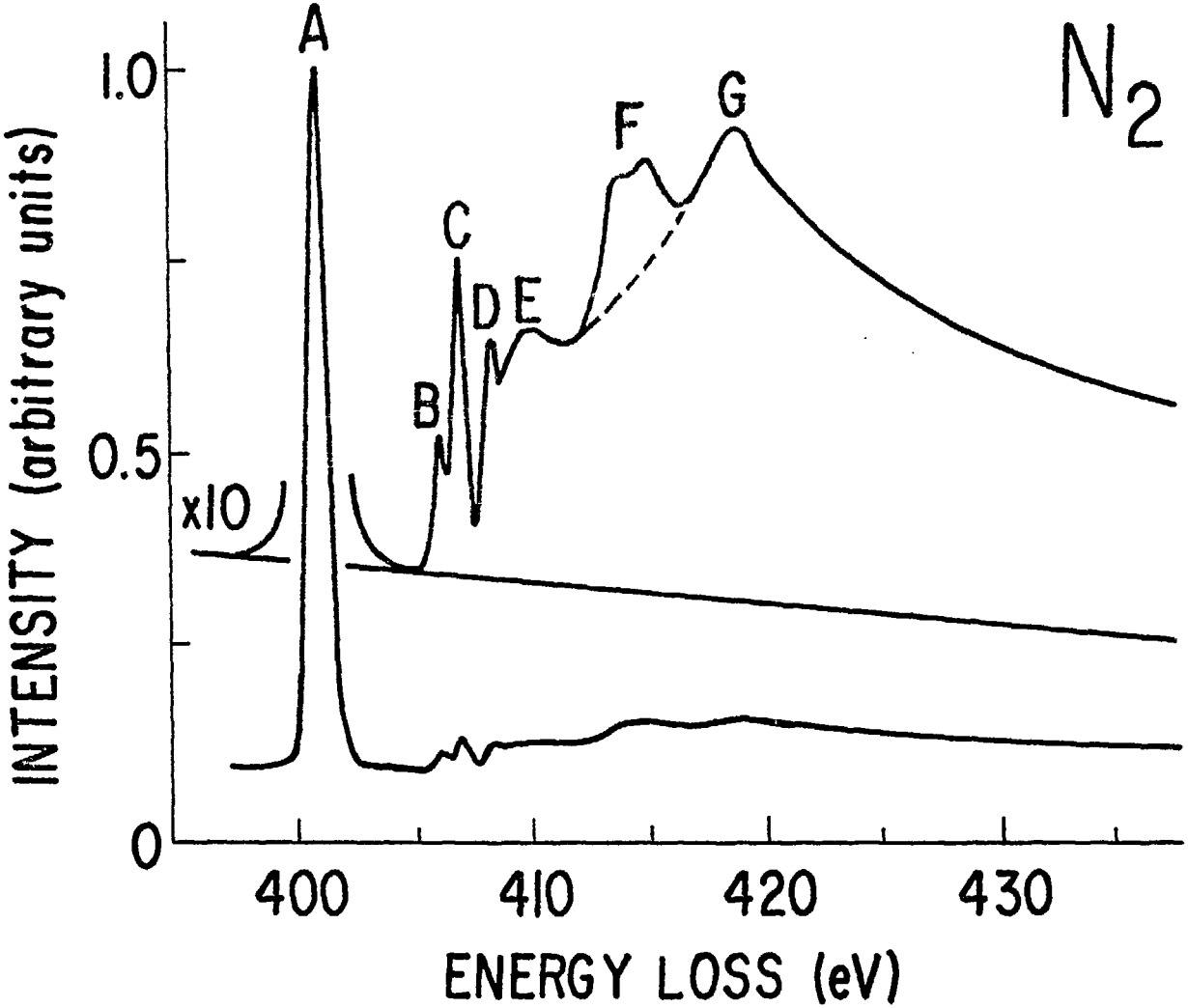
A
B
C
D
E
F
G
N_2
1.0
0.5
0
x10
INTENSITY (arbitrary units)
400
410
420
430
ENERGY LOSS (eV)